A fully coupled chemo-mechanical cohesive zone model for oxygen embrittlement of nickel-based superalloys

J. Mech. Phys. Solids 164 (2022) 104880

Contents lists available at ScienceDirect

Journal of the Mechanics and Physics of Solids

journal homepage: www.elsevier.com/locate/jmps

A fully coupled chemo-mechanical cohesive zone model for oxygen embrittlement of nickel-based superalloys

Kim Louisa Auth [a,*], Jim Brouzoulis [b], Magnus Ekh [a]

[a] Division of Material and Computational Mechanics, Department of Industrial and Materials Science, Chalmers University of Technology, 41296, Sweden

[b] Division of Dynamics, Department of Mechanics and Maritime Sciences, Chalmers University of Technology, 41296, Sweden

ARTICLE INFO

Keywords:
Intergranular fracture
Grain boundaries
Crystal plasticity
Stress-assisted oxidation
Polycrystalline material

ABSTRACT

For nickel-based superalloys subjected to high temperatures and oxygen-rich environments, mechanical loading in combination with oxygen diffusion along grain boundaries leads to an acceleration of crack propagation. To account for these phenomena, a fully coupled thermodynamically consistent chemo-mechanical modeling framework for stress-assisted oxygen embrittlement of grain boundaries in polycrystals is proposed. We formulate an extended cohesive zone model where the grain boundary strength is reduced by the presence of oxygen and the oxygen diffusion is enhanced by tensile mechanical loading. We show that the model can qualitatively predict experimental results such as: reduction of ultimate tensile strength and accelerated crack growth due to dwell time combined with mechanical loading and saturation of crack growth rates for increasing environmental oxygen pressure levels. In addition, numerical simulation results of intergranular crack growth are shown for a 2D polycrystalline structure. An emphasis is put on the difference in cracking behavior after dwelling with or without mechanical loading.

1. Introduction

Nickel-based superalloys are commonly used in gas turbines, for example for jet engines or power generation. In these severe environments, the materials must withstand high temperatures, cyclic loading, and significant dwell times. At high temperatures and in oxygen-rich environments, a shift from transgranular ductile fracture to intergranular brittle fracture, which is accompanied by an acceleration of crack growth, can be observed in nickel-based superalloys. There exist two major theories concerning the physical phenomena behind this behavior, dynamic embrittlement (DE) and stress-assisted grain boundary oxidation (SAGBO). In DE, oxygen molecules diffuse into the grain boundary and therein act as embrittling element see e.g. Liu and White (1987) leading to crack propagation. Opposed to this, in SAGBO brittle fracture of oxygen intrusions at the crack tip exposes new surfaces to further oxidation and continued cracking (discussed e.g. in Bricknell and Woodford (1981)). Within this work, we do not limit ourselves to one of the theories and instead aim to capture experimental observations by our model.

The combination of mechanical load and embrittling species diffusing into grain boundaries or other interfaces, where it ultimately leads to material failure can be observed in a similar way for many other materials, e.g. hydrogen embrittlement of metals, stress-relief cracking in steels or diffusion induced fracture in lithium-ion batteries. A comprehensive overview of intergranular fracture under the influence of stress-assisted diffusion with an emphasis on nickel-based superalloys and on dynamic embrittlement is given by Krupp (2005). To increase the understanding and the possibility to predict these phenomena, development of models

* Corresponding author.
E-mail address: kim.auth@chalmers.se (K.L. Auth).

https://doi.org/10.1016/j.jmps.2022.104880
Received 26 November 2021; Received in revised form 3 March 2022; Accepted 24 March 2022
Available online 21 April 2022

and simulation tools is needed. An early contribution of modeling stress-assisted diffusion can be found in Sofronis and McMeeking (1989) in the context of hydrogen embrittlement. Further cohesive zone models for hydrogen embrittlement have been suggested by Serebrinsky et al. (2004) and by del Busto et al. (2017).

There are numerous models in literature accounting for full chemo-mechanical coupling between different fields, see e.g. Musienko and Cailletaud (2009), Di Leo and Anand (2013) Sedlak et al. (2019). Recently, Kristensen et al. (2020) suggested a framework for a fully chemo-mechanically coupled phase-field model of hydrogen embrittlement including higher-order strain gradient plasticity for accurate predictions of crack-tip stress concentrations. Work on coupled chemo-mechanical cohesive zone formulations for batteries can e.g. be found in Bai et al. (2020) and Rezaei et al. (2021). Particularly, Rezaei et al. (2021) have developed a thermodynamically consistent framework for a fully coupled chemo-mechanical cohesive zone model with an application to solid-state batteries.

In the context of nickel-based superalloys, some finite element modeling of oxygen embrittlement can be found in the literature, e.g. Zhao (2011), Karabela et al. (2013), Sun and Maciejewski (2012). However, in these contributions the full chemo-mechanical coupling is not considered. In Zhao (2011) and Karabela et al. (2013) the mechanical behavior is not affected by the diffusion along grain boundaries while in Sun and Maciejewski (2012) there is no influence of the mechanical problem on the diffusion. Therefore, we propose a modeling framework for fully coupled simulations of stress-assisted oxidation and grain boundary fracture in polycrystals. An important objective of this work is to investigate whether such a model can be used towards predictions and an improved understanding of observations made in experimental work over the past few decades about the interaction between oxygen and mechanical properties in grain boundaries.

For nickel-based superalloys, it has been observed in Liu and White (1987) that there is a loss of ductility and a reduction of ultimate tensile strength in oxygen-rich environments compared to vacuum. However, this is only the case if the material is subjected to tensile mechanical loading during the oxygen exposure (Liu and White, 1987). Furthermore, it has been observed for many years that intergranular crack growth in superalloys at high temperatures is influenced by oxygen-rich environments such as environmental air, in particular an acceleration of crack growth in oxygen-rich environments compared to vacuum can be observed. (e.g. Chang et al. (1990), Andrieu et al. (1992), Pfaendtner and McMahon (2001), Christ et al. (2016)). For high environmental pressure levels, a saturation of the crack-growth rates is observed as described by e.g. Molins et al. (1997), Moverare and Gustafsson (2011), Pfaendtner and McMahon (2001) and Christ et al. (2016). Opposed to hydrogen embrittlement, oxygen can be found exclusively along intergranular cracks and in a small region of the grain boundary ahead of the crack tip in nickel-based superalloys (Hörnqvist et al., 2014), Viskari et al. (2013). In this work we focus on intergranular crack-growth due to oxygen embrittlement. Thereby, the possible crack-growth paths are limited to grain boundaries and it is a compelling choice to use cohesive zone modeling. As the oxygen diffusion seems to be limited to the grain boundaries, it is reasonable to restrict the concentration field to the grain boundaries as well.

Furthermore, we develop a thermodynamically consistent chemo-mechanically coupled cohesive zone model for stress-assisted diffusion of oxygen into grain boundaries followed by intergranular fracture. The fully coupled model captures mechanical degradation of grain boundaries by oxygen as well as mechanically driven diffusion of oxygen ahead of the crack-tip. Opposed to previous suggestions found in the literature, we suggest a model where the oxygen diffusion is accelerated by the gradient of normal traction in the cohesive zone and not by the extrapolated gradient of the hydrostatic stress, as e.g. in del Busto et al. (2017).

The developed model allows for mixed-mode loading/unloading scenarios and can thus be used for cyclic loading scenarios. A fully chemo-mechanically coupled cohesive finite element formulation is presented and a monolithic algorithm is adopted to solve the resulting equations. Finally, we show by numerical experiments on a model problem and a polycrystalline problem that the proposed formulation gives qualitatively reasonable predictions of experimental results for stress-assisted oxidation in polycrystalline nickel-based superalloys.

2. Coupled chemo-mechanical model

The aim of this work is to present a model for oxygen-assisted fracture along the grain boundaries in polycrystals. We assume that the grains experience solely mechanical deformation, while both mechanical deformation and oxygen diffusion occur along the grain boundaries. The mechanical behavior of the grain boundaries is captured by cohesive zone modeling. Analogously, a cohesive zone like approach is developed for modeling the diffusion process.

2.1. Kinematics

Consider a polycrystal as illustrated in Fig. 1. The grains constitute the bulk domain Ω and the grain boundaries the cohesive surface domain Γ_s. The kinematic variables of the problem at hand are then the displacement field $\boldsymbol{u}(\boldsymbol{X},t)$ where $\boldsymbol{X} \in \Omega \cup \Gamma_s$ and the oxide concentration (mass per unit area) field in the grain boundaries $c^{gb}(\boldsymbol{X},t)$ where $\boldsymbol{X} \in \Gamma_s$. In the grains, we make use of the linear strain tensor $\boldsymbol{\varepsilon}$

$$\boldsymbol{\varepsilon} = \frac{1}{2}\left(\boldsymbol{\nabla} \otimes \boldsymbol{u} + \boldsymbol{u} \otimes \boldsymbol{\nabla}\right). \tag{1}$$

The displacement jump cross the grain boundaries $\boldsymbol{\Delta}$ is defined as

$$\boldsymbol{\Delta} = \boldsymbol{u}_+ - \boldsymbol{u}_-, \tag{2}$$

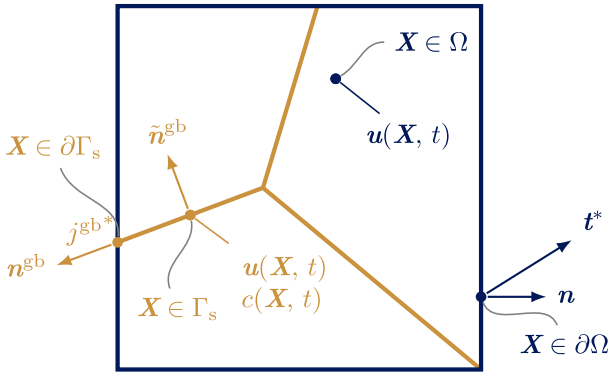

Fig. 1. Polycrystalline domain consisting of the bulk domain Ω and the cohesive domain Γ_s and their respective boundaries $\partial\Omega$ and $\partial\Gamma_\mathrm{s}$. The displacement field $\boldsymbol{u}$ is defined on Ω and on Γ_s, while the concentration field c is defined only on Γ_s.

with $\boldsymbol{u}_+$ and $\boldsymbol{u}_-$ denoting the displacements at opposite sides of the grain boundary. The normal displacement jump Δ_n can by assuming that $\tilde{\boldsymbol{n}}^\mathrm{gb}$ denotes the unit normal to the grain boundary (compare Fig. 1) be computed as

$$\Delta_\mathrm{n} = \boldsymbol{\Delta} \cdot \tilde{\boldsymbol{n}}^\mathrm{gb}\,, \tag{3}$$

the in-plane (tangential) jump $\boldsymbol{\Delta}_\mathrm{t}$ is then obtained as

$$\boldsymbol{\Delta}_\mathrm{t} = \boldsymbol{\Delta} - \Delta_\mathrm{n}\,\tilde{\boldsymbol{n}}^\mathrm{gb} = \left(\boldsymbol{I} - \tilde{\boldsymbol{n}}^\mathrm{gb} \otimes \tilde{\boldsymbol{n}}^\mathrm{gb}\right) \cdot \boldsymbol{\Delta}\,. \tag{4}$$

The oxygen diffusion along the grain boundaries is driven by the chemical potential μ. Assuming a relation according to Fick's first law, the oxygen flux in the grain boundaries $\boldsymbol{j}^\mathrm{gb}$ is given by

$$\boldsymbol{j}^\mathrm{gb} = -\frac{D\,c^\mathrm{gb}}{\mathrm{R}\,T}\,\boldsymbol{\nabla}^\mathrm{gb}\mu\,, \tag{5}$$

where D is the oxygen diffusion coefficient, R is the universal gas constant and T is the absolute temperature. Furthermore, the gradient operator on the cohesive surface is defined as

$$\boldsymbol{\nabla}^\mathrm{gb} = \left(\boldsymbol{I} - \tilde{\boldsymbol{n}}^\mathrm{gb} \otimes \tilde{\boldsymbol{n}}^\mathrm{gb}\right) \cdot \boldsymbol{\nabla}\,. \tag{6}$$

2.2. Balance equations

In the grains Ω, the balance of linear momentum under quasi-static conditions without body forces is given as

$$\boldsymbol{\nabla} \cdot \boldsymbol{\sigma} = \boldsymbol{0}\,. \tag{7}$$

On the grain boundary domain Γ_s both the balance of linear momentum and the conservation of oxide mass must be fulfilled. If $\boldsymbol{T}_+$ and $\boldsymbol{T}_-$ are the traction vectors on opposite sides of the grain boundaries, the balance of linear momentum is given by

$$\boldsymbol{T}_+ + \boldsymbol{T}_- = \boldsymbol{0}\,, \tag{8}$$

and the conservation of oxide mass in the absence of source terms is given by

$$\dot{c}^\mathrm{gb} = -\boldsymbol{\nabla}^\mathrm{gb} \cdot \boldsymbol{j}^\mathrm{gb}\,. \tag{9}$$

2.3. Dissipation inequality

In the grains Ω, the second law of thermodynamics follows a standard format for a purely mechanical problem

$$\boldsymbol{\sigma} : \dot{\boldsymbol{\varepsilon}} - \dot{\Psi}_\Omega \geq 0\,, \tag{10}$$

where $\boldsymbol{\sigma} : \dot{\boldsymbol{\varepsilon}}$ is the mechanical power supply and Ψ_Ω is the free energy per unit volume, which will be introduced in Section 4.

For deriving the dissipation inequality on the grain boundaries Γ_s we follow the procedure in Gurtin et al. (2010). The supply of chemical power P^chem on the grain boundaries is obtained as

$$P^\mathrm{chem} = \int_{\Gamma_\mathrm{s}} \mu\,\dot{c}^\mathrm{gb}\,\mathrm{d}A - \int_{\Gamma_\mathrm{s}} \boldsymbol{\nabla}^\mathrm{gb}\,\mu \cdot \boldsymbol{j}^\mathrm{gb}\,\mathrm{d}A\,. \tag{11}$$

The supply of mechanical power in the grain boundaries P^coh is given by (see e.g. Ottosen et al. (2015))

$$P^\mathrm{coh} = \int_{\Gamma_\mathrm{s}} \boldsymbol{T}_+ \cdot \dot{\boldsymbol{u}}_+ + \boldsymbol{T}_- \cdot \dot{\boldsymbol{u}}_-\,\mathrm{d}A = \int_{\Gamma_\mathrm{s}} \boldsymbol{T} \cdot \dot{\boldsymbol{\Delta}}\,\mathrm{d}A\,, \tag{12}$$

where $\boldsymbol{T} = \boldsymbol{T}_+ = -\boldsymbol{T}_-$. The dissipation inequality for the proposed coupled model follows from introducing Eqs. (11) and (12) as

$$-\dot{\Psi}_{\Gamma_s} + \mathbf{T}\cdot\dot{\boldsymbol{\Delta}} + \mu\,\dot{c}^{\mathrm{gb}} - \boldsymbol{\nabla}^{\mathrm{gb}}\mu\cdot\boldsymbol{j}^{\mathrm{gb}} \geq 0\,. \tag{13}$$

Note that the free energy Ψ_{Γ_s} is an energy per unit grain boundary area. We assume a free energy of the form

$$\Psi_{\Gamma_s} = \Psi_{\Gamma_s}\left(c^{\mathrm{gb}},\,\Delta_{\mathrm{n}},\,\boldsymbol{\Delta}_{\mathrm{t}},\,\boldsymbol{d}_{\mathrm{x}}\right)\,, \tag{14}$$

where $\boldsymbol{d}_{\mathrm{x}}$ denotes a set of independent damage variables. The traction vector $\boldsymbol{T}$ is decomposed in the same manner as the separation jump, i.e.

$$T_{\mathrm{n}} = \boldsymbol{T}\cdot\tilde{\boldsymbol{n}}^{\mathrm{gb}}, \qquad \boldsymbol{T}_{\mathrm{t}} = \left(\boldsymbol{I} - \tilde{\boldsymbol{n}}^{\mathrm{gb}}\otimes\tilde{\boldsymbol{n}}^{\mathrm{gb}}\right)\cdot\boldsymbol{T}\,, \tag{15}$$

whereby $\boldsymbol{T}\cdot\boldsymbol{\Delta} = T_{\mathrm{n}}\,\Delta_{\mathrm{n}} + \boldsymbol{T}_{\mathrm{t}}\cdot\boldsymbol{\Delta}_{\mathrm{t}}$. Introducing Eq. (14) into Eq. (13), the dissipation inequality can be rewritten as

$$\left(T_{\mathrm{n}} - \frac{\partial\Psi_{\Gamma_s}}{\partial\Delta_{\mathrm{n}}}\right)\dot{\Delta}_{\mathrm{n}} + \left(\boldsymbol{T}_{\mathrm{t}} - \frac{\partial\Psi_{\Gamma_s}}{\partial\boldsymbol{\Delta}_{\mathrm{t}}}\right)\cdot\dot{\boldsymbol{\Delta}}_{\mathrm{t}} + \left(\mu - \frac{\partial\Psi_{\Gamma_s}}{\partial c^{\mathrm{gb}}}\right)\dot{c}^{\mathrm{gb}} - \left(\frac{\partial\Psi_{\Gamma_s}}{\partial\boldsymbol{d}_{\mathrm{x}}}\right)^{\mathrm{T}}\dot{\boldsymbol{d}}_{\mathrm{x}} - \boldsymbol{\nabla}^{\mathrm{gb}}\mu\cdot\boldsymbol{j}^{\mathrm{gb}} \geq 0\,. \tag{16}$$

As $\dot{\Delta}_{\mathrm{n}}$, $\dot{\boldsymbol{\Delta}}_{\mathrm{t}}$ and $\dot{c}^{\mathrm{gb}}$ are arbitrary, the following relations can be concluded from Eq. (16)

$$T_{\mathrm{n}} = \frac{\partial\Psi_{\Gamma_s}}{\partial\Delta_{\mathrm{n}}}\,, \quad \boldsymbol{T}_{\mathrm{t}} = \frac{\partial\Psi_{\Gamma_s}}{\partial\boldsymbol{\Delta}_{\mathrm{t}}}\,, \quad \mu = \frac{\partial\Psi_{\Gamma_s}}{\partial c^{\mathrm{gb}}}\quad. \tag{17}$$

From Eq. (5) we conclude that $-\boldsymbol{\nabla}^{\mathrm{gb}}\mu\cdot\boldsymbol{j}^{\mathrm{gb}} \geq 0$. It follows that the dissipation inequality is fulfilled if

$$-\left(\frac{\partial\Psi_{\Gamma_s}}{\partial\boldsymbol{d}_{\mathrm{x}}}\right)^{\mathrm{T}}\dot{\boldsymbol{d}}_{\mathrm{x}} \geq 0\,. \tag{18}$$

3. Coupled constitutive model for grain boundaries

In this section, a fully coupled chemo-mechanical cohesive law is proposed by introducing Ψ_{Γ_s} part by part. The different parts of the model are motivated from experimental observations.

3.1. Base cohesive law

The mechanical behavior of the grain boundaries is modeled by cohesive zone modeling. As the underlying cohesive law, the Xu–Needleman traction-separation law (Xu and Needleman, 1993) is used. However, the Xu–Needleman law is reversible upon unloading. In order to overcome this limitation and allow for realistic cyclic loading, we follow the proposal by Kolluri et al. (2014) and apply an irreversible damage unloading framework to the suggested modified version of the Xu–Needleman cohesive law. The formulation is extended to be applicable in 3D space. The base cohesive tractions $\boldsymbol{T}^{\mathrm{base}} = \left[\boldsymbol{T}_{\mathrm{t}}^{\mathrm{base}},\,T_{\mathrm{n}}^{\mathrm{base}}\right]$ are given by

$$\boldsymbol{T}_{\mathrm{t}}^{\mathrm{base}} = K_{\mathrm{t}}\,\boldsymbol{\Delta}_{\mathrm{t}}\,, \qquad T_{\mathrm{n}}^{\mathrm{base}} = K_{\mathrm{n}}\,\Delta_{\mathrm{n}}\,, \tag{19}$$

where the cohesive stiffnesses K_{t} and K_{n} are defined as follows

$$\begin{aligned} K_{\mathrm{t}} &= \frac{\boldsymbol{\Phi}_{\mathrm{t}}}{\delta_{\mathrm{t}}^2}\,(1-d_{\mathrm{t}})\,(1-d_{\mathrm{c,n}})\,,\\ K_{\mathrm{n}} &= \frac{\boldsymbol{\Phi}_{\mathrm{n}}}{\delta_{\mathrm{n}}^2}\,\left(1-d_{\mathrm{n}}\,\mathcal{H}\left(\Delta_{\mathrm{n}}\right)\right)\,\left(1-d_{\mathrm{c,t}}\,\mathcal{H}\left(\Delta_{\mathrm{n}}\right)\right)\,. \end{aligned} \tag{20}$$

Therein, $\boldsymbol{\Phi}_{\mathrm{n}}$ / $\boldsymbol{\Phi}_{\mathrm{t}}$ are the normal/tangential work of separation and δ_{n} / δ_{t} are the normal/tangential characteristic separations. The Heaviside step function $\mathcal{H}$ is used to restrict the influence of damage on $T_{\mathrm{n}}^{\mathrm{base}}$ to situations with positive normal displacement jump. Within the cohesive plane, isotropy is assumed. Furthermore, the damage variables d_{n}, $d_{\mathrm{c,t}}$, d_{t} and $d_{\mathrm{c,n}}$ are introduced as

$$\begin{aligned} d_{\mathrm{n}} &= 1-\exp\left(-\frac{\Delta_{\mathrm{n,max}}}{\delta_{\mathrm{n}}}\right)\,, \quad d_{\mathrm{c,t}} = 1-\exp\left(-\frac{\Delta_{\mathrm{t,max}}^2}{2\,\delta_{\mathrm{t}}^2}\right)\,,\\ d_{\mathrm{t}} &= 1-\exp\left(-\frac{\Delta_{\mathrm{t,max}}^2}{2\,\delta_{\mathrm{t}}^2}\right)\,, \quad d_{\mathrm{c,n}} = 1-\left(1+\frac{\Delta_{\mathrm{n,max}}}{\delta_{\mathrm{n}}}\right)\exp\left(-\frac{\Delta_{\mathrm{n,max}}}{\delta_{\mathrm{n}}}\right)\,, \end{aligned} \tag{21}$$

with the history variables $\Delta_{\mathrm{t,max}}$ and $\Delta_{\mathrm{n,max}}$, which represent the maximum displacement jumps experienced in the tangential and normal directions, respectively. Damage growth is controlled by the Karush–Kuhn–Tucker conditions, which ensure that damage does not evolve during unloading or for a negative normal displacement jump

$$\begin{aligned} &\dot{\Delta}_{\mathrm{n,max}} \geq 0\,, \quad \dot{\Delta}_{\mathrm{n,max}}\,f_{\mathrm{n}} = 0\,, \quad f_{\mathrm{n}} = \Delta_{\mathrm{n}} - \Delta_{\mathrm{n,max}} \leq 0\,,\\ &\dot{\Delta}_{\mathrm{t,max}} \geq 0\,, \quad \dot{\Delta}_{\mathrm{t,max}}\,f_{\mathrm{t}} = 0\,, \quad f_{\mathrm{t}} = |\boldsymbol{\Delta}_{\mathrm{t}}| - \Delta_{\mathrm{t,max}} \leq 0\,. \end{aligned} \tag{22}$$

3.2. Coupled cohesive law

In order to model the reduction of strength in presence of oxygen (Liu and White, 1987), an environmental damage variable d_{O_2} is introduced. It reduces the base cohesive tractions $\boldsymbol{T}^{\mathrm{base}}$ such that the environmentally degraded traction $\hat{\boldsymbol{T}} = \left[\hat{T}_{\mathrm{t}}, \hat{T}_{\mathrm{n}}\right]$ is obtained as

$$\hat{\boldsymbol{T}} = \left(1 - d_{\mathrm{O}_2}\, \mathcal{H}(\Delta_{\mathrm{n}})\right) \boldsymbol{T}^{\mathrm{base}}\,. \tag{23}$$

Hence, for positive normal separation the environmental damage variable d_{O_2} results in a reduced ultimate strength and a reduced cohesive stiffness which lead to faster crack propagation. The next step is to define a relation between the environmental damage d_{O_2} and the oxygen concentration c. We introduce the maximum experienced concentration $c^{\mathrm{gb}}_{\mathrm{max}}$ as a history variable for each point along the grain boundaries. This can also be expressed as

$$\dot{c}^{\mathrm{gb}}_{\mathrm{max}} \geq 0\,, \quad \dot{c}^{\mathrm{gb}}_{\mathrm{max}}\, f^{\mathrm{gb}}_{\mathrm{c}} = 0\,, \quad f^{\mathrm{gb}}_{\mathrm{c}} = c^{\mathrm{gb}} - c^{\mathrm{gb}}_{\mathrm{max}} \leq 0\,. \tag{24}$$

Now, remember that we want to replicate experimental results in e.g. Molins et al. (1997) and obtain saturation of the crack propagation rate for cases of high environmental oxygen pressures and/or for long dwell times. Both of these conditions lead to an elevated oxygen level in the grain boundaries. We assume that around a characteristic oxygen concentration $c^{\mathrm{gb}}_{\mathrm{char}}$ the environmental damage depends on the oxygen concentration, while several times above $c^{\mathrm{gb}}_{\mathrm{char}}$ a maximum impact of oxygen on the material is approached. Motivated by this, the environmental damage is chosen as an exponential function

$$d_{\mathrm{O}_2}\left(c^{\mathrm{gb}}_{\mathrm{max}}\right) = d_{\mathrm{O}_2,\mathrm{max}}\left(1 - \exp\left(-\frac{c^{\mathrm{gb}}_{\mathrm{max}}}{c^{\mathrm{gb}}_{\mathrm{char}}}\right)\right), \tag{25}$$

where $d_{\mathrm{O}_2,\mathrm{max}}$ is a model parameter that limits how much the grain boundaries can be degraded by environmental damage.

Similar approaches for modeling environmental degradation have been chosen e.g. by del Busto et al. (2017) or Sun and Maciejewski (2012). In both references damage variables for mechanical and environmental damage are concatenated. Sun and Maciejewski have adopted a linear relation between the oxygen concentration and the damage variable.

Finally, to obtain the traction $\hat{\boldsymbol{T}}$ in Eq. (23) the free energy for the coupled cohesive law Ψ^{coh} is formulated as

$$\Psi^{\mathrm{coh}}\left(\boldsymbol{\Delta}, d_{\mathrm{O}_2}, d_{\mathrm{n}}, d_{\mathrm{c,t}}, d_{\mathrm{t}}, d_{\mathrm{c,n}}\right) = \left(1 - d_{\mathrm{O}_2}\, \mathcal{H}\left(\Delta_{\mathrm{n}}\right)\right)\left(\frac{1}{2}\, K_{\mathrm{n}}\, \Delta_{\mathrm{n}}^2 + \frac{1}{2}\, K_{\mathrm{t}}\, \boldsymbol{\Delta}_{\mathrm{t}} \cdot \boldsymbol{\Delta}_{\mathrm{t}}\right). \tag{26}$$

3.3. Base chemical potential

The chemical potential μ for a diffusion process is given by (similar to e.g. Sofronis and McMeeking (1989))

$$\mu = \mu_0 + \mathrm{R}\, T\, \ln\left(\frac{\theta_{\mathrm{L}}}{1 - \theta_{\mathrm{L}}}\right), \tag{27}$$

where μ_0 is the reference chemical potential, R the universal gas constant, T the absolute temperature and $\theta_{\mathrm{L}} = c^{\mathrm{gb}}/N^{\mathrm{gb}}$ the lattice site occupancy. N^{gb} is the number of lattice sites per grain boundary area. In order to obtain the chemical potential μ given by Eq. (17), the chemical free energy Ψ^{chem} is chosen as

$$\Psi^{\mathrm{chem}}\left(c^{\mathrm{gb}}\right) = \mu_0\, c^{\mathrm{gb}} + \mathrm{R}\, T\, N^{\mathrm{gb}}\, \left(\theta_{\mathrm{L}}\, \ln(\theta_{\mathrm{L}}) + (1 - \theta_{\mathrm{L}})\, \ln(1 - \theta_{\mathrm{L}})\right). \tag{28}$$

3.4. Coupled chemical potential

Liu and White (1987) have shown that if a specimen is exposed to an oxygen rich environment, this alone does not reduce ductility and ultimate strength. To obtain an influence on the material degradation, the specimen must also be mechanically loaded during the oxygen exposure. In order to account for this in the model, we introduce an additional stress dependent part of the chemical potential μ_σ. A commonly adopted model for μ_σ in the context of hydrogen embrittlement is to include a part that is proportional to the hydro-static stress (see e.g. Sofronis and McMeeking (1989), Serebrinsky et al. (2004), del Busto et al. (2017), Kristensen et al. (2020)). The underlying assumption is that the embrittling species causes a pure dilatational strain. However, as the concentration field is limited to the cohesive zones in our modeling, this is not a natural choice, as the hydrostatic stress is not readily available in cohesive elements. As volumetric deformation in cohesive zone modeling is caused only by the normal traction, we analogously suggest that the stress-dependent chemical potential μ_σ is proportional to the normal traction component T_{n}. With V_{O_2} being the partial molar volume of oxygen in metal, the stress – or rather traction – dependent chemical potential then reads

$$\mu_\sigma = -V_{\mathrm{O}_2}\, \hat{T}_{\mathrm{n}}\,. \tag{29}$$

It causes an additional term in the oxygen flux $\boldsymbol{j}^{\mathrm{gb}}$ that increases the flux towards high normal tractions and reduces oxygen flux towards regions with low normal tractions. To obtain the stress-dependent chemical potential μ_σ, the free energy for traction assisted oxygen diffusion Ψ^{coupling} is chosen as

$$\Psi^{\mathrm{coupling}}\left(c^{\mathrm{gb}}, \Delta_{\mathrm{n}}, d_{\mathrm{O}_2}, d_{\mathrm{n}}, d_{\mathrm{c,t}}\right) = -V_{\mathrm{O}_2}\, \hat{T}_{\mathrm{n}}\, (c^{\mathrm{gb}} - c^{\mathrm{gb}}_0), \tag{30}$$

where c^{gb}_0 is a reference grain boundary concentration.

3.5. Chemo-mechanically coupled free energy for grain boundaries

The complete free energy Ψ_{Γ_s} for the fully coupled chemo-mechanical cohesive model is given by

$$\Psi_{\Gamma_s} = \Psi^{\text{coh}} + \Psi^{\text{chem}} + \Psi^{\text{coupling}} . \tag{31}$$

The cohesive tractions $\boldsymbol{T} = \left[\boldsymbol{T}_{\text{t}}, T_{\text{n}}\right]$ then follow from Eq. (17) as

$$\begin{aligned} \boldsymbol{T}_{\text{t}} &= \left(1 - d_{\text{O}_2}\, \mathcal{H}\left(\Delta_{\text{n}}\right)\right) K_{\text{t}}\, \boldsymbol{\Delta}_{\text{t}} , \\ T_{\text{n}} &= \left(1 - d_{\text{O}_2}\, \mathcal{H}\left(\Delta_{\text{n}}\right)\right) K_{\text{n}} \left(\Delta_{\text{n}} - V_{\text{O}_2}\,(c^{\text{gb}} - c_0^{\text{gb}})\right) . \end{aligned} \tag{32}$$

While the tangential traction $\boldsymbol{T}_{\text{t}}$ results solely from Ψ^{coh}, the normal traction T_{n} has contributions from Ψ^{coh}, represented by Δ_{n} in the last parenthesis of Eq. (32), and Ψ^{coupling}, represented by $V_{\text{O}_2}\,(c^{\text{gb}} - c_0^{\text{gb}})$ respectively. Notice that the latter can be physically described as a contribution to the normal separation (volume expansion) due to the presence of oxygen. With the set of parameters applied in Section 6, the coupling contribution to the normal separation has an upper bound of $0.209 \cdot 10^{-9}$ mm, which corresponds to 0.0014% of the characteristic normal separation jump δ_{n} is thus negligible for this case. The term is however not neglected from the model formulation and its numerical treatment, as it might be relevant for a different set of parameter values, in particular for larger values of the cohesive zone thickness h (introduced in Section 5.2).

The chemical potential μ can be derived from Eq. (17) as

$$\mu = \mu_0 + \text{RT}\, \ln\left(\frac{\theta_{\text{L}}}{1 - \theta_{\text{L}}}\right) - V_{\text{O}_2} \left(1 - d_{\text{O}_2}\, \mathcal{H}\left(\Delta_{\text{n}}\right)\right) K_{\text{n}}\, \Delta_{\text{n}} . \tag{33}$$

We assume that the lattice occupancy θ_{L} is low ($\theta_{\text{L}} \ll 1$) and that the concentration of interstitial lattice sites N^{gb} is constant. These assumptions are often adopted see e.g. Kristensen et al. (2020), Sofronis and McMeeking (1989). By inserting Eq. (33) into Eq. (5) we finally obtain the following expression for the oxygen flux

$$\boldsymbol{j}^{\text{gb}} = -D\, \boldsymbol{\nabla}^{\text{gb}} c^{\text{gb}} + D\, c^{\text{gb}}\, \frac{V_{\text{O}_2}}{\text{R}\, T}\, \boldsymbol{\nabla}^{\text{gb}} \hat{T}_{\text{n}} . \tag{34}$$

In Appendix A it is shown that the grain boundary model is in general thermodynamically consistent.

4. Constitutive model for grains

The grains are modeled by a crystal plasticity model with linear isotropic and non-linear kinematic hardening. For completeness, the crystal plasticity model is briefly described in this section.

We adopt an additive split of the strain tensor $\boldsymbol{\varepsilon}$ into an elastic part $\boldsymbol{\varepsilon}^{\text{e}}$ and a plastic part $\boldsymbol{\varepsilon}^{\text{p}}$

$$\boldsymbol{\varepsilon} = \boldsymbol{\varepsilon}^{\text{e}} + \boldsymbol{\varepsilon}^{\text{p}} . \tag{35}$$

The free energy per unit bulk volume Ψ_{Ω} is introduced as

$$\Psi_{\Omega} = \frac{1}{2}\, \boldsymbol{\varepsilon}^{\text{e}} : \mathbf{E} : \boldsymbol{\varepsilon}^{\text{e}} + \sum_{\alpha=1}^{N_\alpha} \frac{1}{2} H_{\text{iso}}\, k_\alpha^2 + \sum_{\alpha=1}^{N_\alpha} \frac{1}{2} H_{\text{kin}}\, b_\alpha^2 , \tag{36}$$

where $\mathbf{E}$ is the elastic stiffness tensor, while H_{iso} and H_{kin} denote the isotropic and kinematic hardening moduli. Further, k_α and b_α represent the isotropic and kinematic hardening variables of the α-th slip system. Thus the stress $\boldsymbol{\sigma}$ and the thermodynamic stresses κ_α and β_α are obtained as

$$\boldsymbol{\sigma} = \mathbf{E} : \boldsymbol{\varepsilon}^{\text{e}} , \qquad \kappa_\alpha = -H_{\text{iso}}\, k_\alpha , \qquad \beta_\alpha = -H_{\text{kin}}\, b_\alpha . \tag{37}$$

The yield function for each slip system $\boldsymbol{\Phi}_\alpha$ is given by

$$\boldsymbol{\Phi}_\alpha(\boldsymbol{\sigma}, \beta_\alpha, \kappa_\alpha) = |\tau_\alpha - \beta_\alpha| - \kappa_\alpha - \tau_{\text{y}} , \tag{38}$$

where τ_{y} is the yield limit. The effective stress used in $\boldsymbol{\Phi}_\alpha$ is the Schmid stress τ_α. It is obtained by the projection of the stress $\boldsymbol{\sigma}$ onto the α-th slip system. Each slip system is characterized by a slip direction $\boldsymbol{s}_\alpha$ and the normal vector to the slip plane $\boldsymbol{m}_\alpha$. The Schmid stress τ_α is thereby obtained as

$$\tau_\alpha = \boldsymbol{\sigma} : \left(\boldsymbol{s}_\alpha \otimes \boldsymbol{m}_\alpha\right) . \tag{39}$$

An associative evolution equation is adopted for the plastic strain $\boldsymbol{\varepsilon}^{p}$

$$\dot{\boldsymbol{\varepsilon}}^{p} = \sum_{\alpha=1}^{N_\alpha} \dot{\lambda}_\alpha\, \frac{\partial \boldsymbol{\Phi}_\alpha}{\partial \boldsymbol{\sigma}} , \tag{40}$$

and linear hardening law for the isotropic hardening

$$\dot{k}_\alpha = -\dot{\lambda}_\alpha , \tag{41}$$

are employed. For the kinematic hardening we adopt a saturation type of evolution equation (compare Meyer (2020), Méric et al. (1991))

$$\dot{b}_\alpha = -\left(\operatorname{sign}\left(\tau_\alpha - \beta_\alpha\right) - \frac{\beta_\alpha}{\beta_\infty}\right)\dot{\lambda}_\alpha\,. \tag{42}$$

The multiplier $\dot{\lambda}_\alpha$ is defined by visco-plastic regularization, where t^*, m and σ_d are parameters controlling the viscosity of the model.

$$\dot{\lambda}_\alpha = \frac{1}{\mathrm{t}^*}\left\langle\frac{\Phi_\alpha}{\sigma_\mathrm{d}}\right\rangle^m\,. \tag{43}$$

5. Finite element formulation

In the following section, we discuss some practical aspects of solving the balance equation presented in Section 2.2. The chemical conservation of mass, Eq. (9), is time-discretized by a backward Euler scheme such that

$${}^{n+1}c^{\mathrm{gb}} - {}^{n}c^{\mathrm{gb}} = -\Delta t\,\nabla^{\mathrm{gb}}\cdot{}^{n+1}\boldsymbol{j}^{\mathrm{gb}}\,, \tag{44}$$

where ${}^{n+1}c^{\mathrm{gb}}$ and ${}^{n}c^{\mathrm{gb}}$ are the concentrations in the current and previous time step, respectively, ${}^{n+1}\boldsymbol{j}^{\mathrm{gb}}$ is the oxygen flux in the current time step, and Δt is the time increment. Subsequently the superscript $n+1$ is omitted and all variables without indication of the time step refer to the current step.

5.1. Weak form of balance equations

After introducing test functions δc and $\delta\boldsymbol{u}$, the weak form of the time-discretized mass balance, Eq. (44), can be obtained as

$$\int_{\Gamma_\mathrm{s}}\left(c^{\mathrm{gb}} - {}^{n}c^{\mathrm{gb}}\right)\delta c\,\mathrm{d}A = -\Delta t\left(\int_{\partial\Gamma_\mathrm{s}}\boldsymbol{j}^{\mathrm{gb}}\cdot\boldsymbol{n}^{\mathrm{gb}}\,\delta c\,\mathrm{d}S - \int_{\Gamma_\mathrm{s}}\boldsymbol{j}^{\mathrm{gb}}\cdot\nabla^{\mathrm{gb}}\delta c\,\mathrm{d}A\right)\,, \tag{45}$$

where $\boldsymbol{n}^{\mathrm{gb}}$ is the unit normal to the boundary of the cohesive interface domain $\partial\Gamma_\mathrm{s}$. Similarly, the unit normal to the boundary of the bulk domain $\partial\Omega$ is called $\boldsymbol{n}$ (compare with Fig. 1). The principle of virtual work then gives the weak form of the mechanical balance equation as

$$\int_\Omega\boldsymbol{\sigma}:\delta\boldsymbol{\varepsilon}\,\mathrm{d}V + \int_{\Gamma_\mathrm{s}}\boldsymbol{T}\cdot\delta\boldsymbol{\Delta}\,\mathrm{d}A = \int_{\partial\Omega}(\boldsymbol{\sigma}\cdot\boldsymbol{n})\cdot\delta\boldsymbol{u}\,\mathrm{d}A\,. \tag{46}$$

Note that the test functions must follow the kinematic field equations and thus $\delta\boldsymbol{\varepsilon}$ and $\delta\boldsymbol{\Delta}$ are functions of $\delta\boldsymbol{u}$. At this point, we introduce natural boundary conditions such that with $\boldsymbol{t}^*$ as the external traction vector on the boundaries of the bulk domain and j^* as the external oxygen flux out of the grain boundary domain, the following relations are obtained

$$\begin{aligned}\boldsymbol{\sigma}\cdot\boldsymbol{n} &= \boldsymbol{t}^* \quad \text{on}\,\partial\Omega\,,\\ \boldsymbol{j}^{\mathrm{gb}}\cdot\boldsymbol{n}^{\mathrm{gb}} &= j^{\mathrm{gb}*} \quad \text{on}\,\partial\Gamma_\mathrm{s}\,.\end{aligned} \tag{47}$$

By inserting Eq. (47) into Eqs. (45) and (46), the virtual work can be formulated as internal virtual work δW_{int} and external virtual work δW_{ext}, such that $\delta W_{\mathrm{int}} = \delta W_{\mathrm{ext}}$

$$\begin{aligned}\delta W_{\mathrm{int}} &= \overbrace{\int_\Omega\boldsymbol{\sigma}:\delta\boldsymbol{\varepsilon}\,\mathrm{d}V}^{\delta W_{\mathrm{int}}^{\mathrm{bulk}}} + \overbrace{\int_{\Gamma_\mathrm{s}}\boldsymbol{T}\cdot\delta\boldsymbol{\Delta}\,\mathrm{d}A}^{\delta W_{\mathrm{int}}^{\mathrm{coh}}} + \overbrace{\int_{\Gamma_\mathrm{s}}\left(c^{\mathrm{gb}} - {}^{n}c^{\mathrm{gb}}\right)\delta c\,\mathrm{d}A - \Delta t\int_{\Gamma_\mathrm{s}}\boldsymbol{j}^{\mathrm{gb}}\cdot\nabla^{\mathrm{gb}}\delta c\,\mathrm{d}A}^{\delta W_{\mathrm{int}}^{\mathrm{chem}}}\,,\\ \delta W_{\mathrm{ext}} &= \underbrace{\int_{\partial\Omega}\boldsymbol{t}^*\cdot\delta\boldsymbol{u}\,\mathrm{d}A}_{\delta W_{\mathrm{ext}}^{\mathrm{bulk}}} - \underbrace{\Delta t\int_{\partial\Gamma_\mathrm{s}}j^{\mathrm{gb}*}\,\delta c\,\mathrm{d}S}_{\delta W_{\mathrm{ext}}^{\mathrm{chem}}}\,.\end{aligned} \tag{48}$$

5.2. A coupled displacement–concentration cohesive element

Standard mechanical cohesive elements are evaluated on a (fictitious) mid-surface and it is, therefore, natural to seek a similar formulation for the coupled displacement–concentration cohesive element. We aim to have both the displacement and the concentration field defined in the nodes, rather than the concentrations being defined on a separate mid-plane mesh.

To achieve this, consider the concentration c (per unit volume) expressed in terms of the mid-plane concentration c^{mid} and a concentration jump Δc between the upper and lower surface

$$c\left(\boldsymbol{\xi}\right) = c^{\mathrm{mid}}\left(\xi_1,\xi_2\right) + \Delta c\left(\xi_1,\xi_2\right)\,\frac{\xi_3}{h}\,, \tag{49}$$

where h is the thickness of the cohesive zone that is taken as a constant model parameter. A local coordinate system $\boldsymbol{\xi} = [\xi_1,\xi_2,\xi_3]$ is introduced to describe the interfaces. As shown in Fig. 2, the coordinate axes ξ_1 and ξ_2 span the mid-plane of the cohesive zone, while ξ_3 points in the normal direction to the mid-plane. Here, we assume that the concentration field is linearly dependent on the

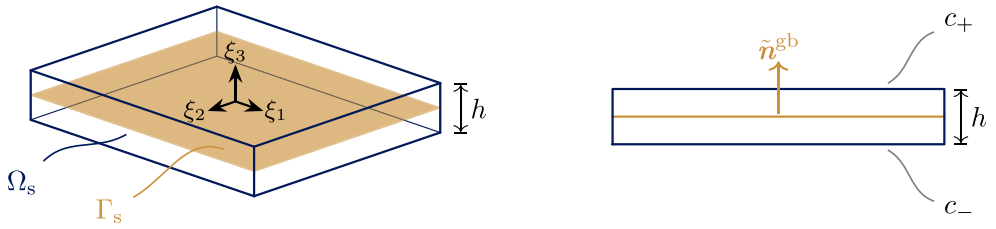

Fig. 2. Representation of a cohesive element with local coordinate system $\boldsymbol{\xi}$, mid-plane domain Γ_s and volume domain Ω_s.

ξ_3-coordinate. By introducing c_+ and c_- as the concentrations at opposite sides of the interface analogously to the displacements $\boldsymbol{u}_+$ and $\boldsymbol{u}_-$, the mid-plane concentration c^{mid} and the concentration jump Δc are obtained as

$$c^{\text{mid}} = \frac{1}{2}\left(c_+ + c_-\right), \qquad \Delta c = c_+ - c_-, \tag{50}$$

where c_+ and c_- are the concentrations on opposite sides of the interface. The variation is chosen in a similar way

$$\delta c\left(\boldsymbol{\xi}\right) = \delta c^{\text{mid}}\left(\xi_1, \xi_2\right) + \delta \Delta c\left(\xi_1, \xi_2\right) \frac{\xi_3}{h}. \tag{51}$$

However, c is a concentration in 3D space, while the material model presented in Section 3 relies on the in-plane concentration c^{gb}. To this end, we establish the relation between c and c^{gb} such that

$$c^{\text{gb}} = \int_{-\frac{h}{2}}^{\frac{h}{2}} c \, \mathrm{d}\xi_3 = h\, c^{\text{mid}}. \tag{52}$$

This leads to the following relations between the in-plane oxygen flux $\boldsymbol{j}^{\text{gb}}$ and the 3D oxygen flux $\boldsymbol{j}$, as well as the external oxygen flux into the mid-plane $j^{\text{gb}*}$, respectively

$$\boldsymbol{j}^{\text{gb}} = \left(\boldsymbol{I} - \tilde{\boldsymbol{n}}^{\text{gb}} \otimes \tilde{\boldsymbol{n}}^{\text{gb}}\right) \cdot h\, \boldsymbol{j}, \qquad j^{\text{gb}*} = h\, j^*. \tag{53}$$

We introduce a thin volume Ω_s around the mid-surface, whose constant thickness is the grain boundary thickness h, and reformulate the time-continuous version of the chemical virtual work δW^{chem} as a volume integral over Ω_s

$$\delta W^{\text{chem}} = \int_{\Omega_s} \dot{c}\, \delta c \, \mathrm{d}V - \int_{\Omega_s} \boldsymbol{j} \cdot \boldsymbol{\nabla} \delta c \, \mathrm{d}V + \int_{\partial\Omega_s} j^*\, \delta c \, \mathrm{d}A. \tag{54}$$

By inserting the expressions for c and δc into Eq. (54), we obtain, as shown in Appendix B, two uncoupled weak forms; one for the grain boundary concentration c^{gb} and one for the concentration jump Δc

$$\int_{\Gamma_s} \dot{c}^{\text{gb}}\, \delta c^{\text{mid}} \, \mathrm{d}A - \int_{\Gamma_s} \boldsymbol{j}^{\text{gb}} \cdot \boldsymbol{\nabla}^{\text{gb}} \delta c^{\text{mid}} \mathrm{d}A + \int_{\partial\Gamma_s} j^{\text{gb}*}\, \delta c^{\text{mid}} \mathrm{d}S = 0, \tag{55}$$

$$\frac{h}{12} \int_{\Gamma_s} \Delta\dot{c}\, \delta \Delta c \, \mathrm{d}A - \int_{\Gamma_s} D\, \frac{\Delta c}{h}\, \delta \Delta c \, \mathrm{d}A - \frac{h}{12} \int_{\Gamma_s} \left(-D\, \boldsymbol{\nabla}^{\text{gb}} \Delta c + \frac{D\, V_{\text{O}_2}}{\mathrm{R}\, T}\, \Delta c\, \boldsymbol{\nabla}^{\text{gb}} \hat{T}_{\text{n}}\right) \cdot \boldsymbol{\nabla}^{\text{gb}} \delta \Delta c \, \mathrm{d}A = 0. \tag{56}$$

Note that Eq. (55) is independent of the chosen model parameter h and is, in fact, identical to (the time continuous version of) Eq. (45). This last result implies that solving the 3D continuity equation, and then extracting the mid surface value, is the same as solving Eq. (45) for c^{gb}; although, at the cost of solving for the unused auxiliary field Δc.

Henceforth, we consider the oxygen concentration as a continuous field defined over the cohesive elements. However, to actually incorporate the model thickness h introduced above, and not the actual thickness defined through the element nodes, we formulate the approximation of the coordinate $\boldsymbol{X}$ as follows

$$\boldsymbol{X} \approx \boldsymbol{X}^{\text{mid}}(\xi_1, \xi_2) + \xi_3\, \tilde{\boldsymbol{n}}^{\text{gb}}(\xi_1, \xi_2), \tag{57}$$

where $\boldsymbol{X}^{\text{mid}}$ is the mid-plane coordinate.

5.3. Finite element discretization

We introduce finite element discretizations such that for a nodal displacement vector $\underline{u}$, a nodal concentration vector $\underline{c}$ and shape function vectors $\underline{\boldsymbol{N}}^{\text{bulk}}$, $\underline{\boldsymbol{N}}^{\text{coh}}$, $\underline{N}^{\text{chem}}$ the fields are approximated as

$$\boldsymbol{u} \approx \underline{u}^{\text{T}}\, \underline{\boldsymbol{N}}^{\text{bulk}}, \qquad \boldsymbol{\Delta} \approx \underline{u}^{\text{T}}\, \underline{\boldsymbol{N}}^{\text{coh}}, \qquad c \approx \underline{c}^{\text{T}}\, \underline{N}^{\text{chem}}. \tag{58}$$

Underscores are used for denoting multidimensional quantities in matrix notation. Notice that the separation jump $\boldsymbol{\Delta}$ depends on the nodal displacements $\underline{u}$. Analogously, the variations $\delta\boldsymbol{u}$, $\delta\boldsymbol{\Delta}$ and δc are approximated as

$$\delta\boldsymbol{u} \approx \underline{\delta u}^{\text{T}}\, \underline{\boldsymbol{N}}^{\text{bulk}}, \qquad \delta\boldsymbol{\Delta} \approx \underline{\delta u}^{\text{T}}\, \underline{\boldsymbol{N}}^{\text{coh}}, \qquad \delta c \approx \underline{\delta c}^{\text{T}}\, \underline{N}^{\text{chem}}. \tag{59}$$

Introducing the FE-approximations into the virtual work, we obtain the out-of-balance vectors $\underline{R}^{\text{mech}}$ and $\underline{R}^{\text{chem}}$ such that

$$\underline{\delta u}^{\mathrm{T}}\,\underline{R}^{\text{mech}} + \underline{\delta c}^{\mathrm{T}}\,\underline{R}^{\text{chem}} = 0\,, \tag{60}$$

which must hold for arbitrary test functions $\delta\boldsymbol{u}$ and δc, leading to

$$R_i^{\text{mech}} = \int_{\Omega} \boldsymbol{\sigma} : \frac{1}{2}\left(\boldsymbol{\nabla}\otimes\boldsymbol{N}_i^{\text{bulk}} + \boldsymbol{N}_i^{\text{bulk}}\otimes\boldsymbol{\nabla}\right)\mathrm{d}V + \int_{\Gamma_{\mathrm{s}}} \boldsymbol{T}\cdot\boldsymbol{N}_i^{\text{coh}}\,\mathrm{d}A - \int_{\partial\Omega} \boldsymbol{t}^{*}\cdot\boldsymbol{N}_i^{\text{bulk}}\,\mathrm{d}A = 0\,, \tag{61}$$

$$R_i^{\text{chem}} = \int_{\Omega_{\mathrm{s}}} \left({}^{n+1}c - {}^{n}c\right) N_i^{\text{chem}}\,\mathrm{d}V + \Delta t \int_{\Omega_{\mathrm{s}}} \boldsymbol{j}\cdot\boldsymbol{\nabla}N_i^{\text{chem}}\,\mathrm{d}V - \Delta t \int_{\partial\Omega_{\mathrm{s}}} j^{*}\,N_i^{\text{chem}}\,\mathrm{d}A = 0\,. \tag{62}$$

Notice that the traction vector $\boldsymbol{T}$ and the flux vector $\boldsymbol{j}$ are functions of the displacements $\boldsymbol{u}$ and the grain boundary concentrations c^{gb}, as well as the state variables $\boldsymbol{\Delta}_{\max}$ and $c^{\text{gb}}_{\max}$. Hence, the resulting equation system is strongly coupled.

For computing the chemical out-of-balance vector, we must find the flux $\boldsymbol{j}$ in the integration points. Determining the flux requires finding the spatial gradient of the normal traction $\hat{T}_{\mathrm{n}} = \hat{T}_{\mathrm{n}}(\Delta_{\mathrm{n}}, \boldsymbol{\Delta}_{\max}, c^{\text{gb}}_{\max})$ (compare Eq. (34)). Therefore, spatial gradients of the history variables are needed. While several ways of obtaining these can be imagined, we aim for a simple approach in this work. For numerical integration, we use a nodal integration scheme with 3 integration points per dimension in the cohesive elements. With this choice, the integration points coincide with the nodal positions of a quadratic Lagrangian interpolation. The (local) spatial gradients in the mid-plane can then conveniently be approximated by using quadratic shape functions with the history variable values from the nodal integration points as nodal values.

5.4. Details of the finite element implementation

The Heaviside function acting on the environmental damage d_{O_2} is regularized such that $\mathcal{H}(\Delta_n) = 1/2 + 1/\pi\,\mathrm{atan}\left(150\,\Delta_{\mathrm{n}}/\delta_{\mathrm{n}}\right)$. The finite element implementation is done in the Julia programming language (Bezanson et al., 2017) by help of the Ferrite.jl finite element package (Carlsson et al., 2021). In addition, the Tensors.jl package (Carlsson and Ekre, 2019) is used, which allows for use of automatic differentiation. A monolithic scheme is employed for solving the coupled system of equations.

6. Numerical results

In this section we present numerical results showing the capabilities of the presented model and the numerical framework. Firstly, a simple problem with two grains and a grain boundary is studied. The focus of this study is to show the interaction between the chemical and mechanical fields. Qualitative comparisons against observations from experiments are conducted. Secondly, the model and the numerical framework are applied to a 2D grain structure. We show the effect of tensile loading during the dwell time on the resulting oxygen distribution in the grain structure. In addition, we analyze the overall macroscopic behavior of the grain structure and its dependence on the mechanical loading as well as the grain boundary diffusion.

For all numerical examples, an average grain size of $150\,\mu\mathrm{m}$ and a mesh size of $3.54\,\mu\mathrm{m}$ have been used. The grains are meshed by CST elements, while the grain boundaries are meshed by linear cohesive elements with 3 Gauss–Lobatto integration points. The plane strain assumption is applied for all numerical examples. Time steps of $0.5\,\mathrm{s}$ during loading periods and $200\,\mathrm{s}$ during dwelling periods are used. The initial oxygen concentration in the grain boundaries is $0.0\,\mathrm{mol/mm^3}$. For numerical reasons, the initial oxygen concentration near the oxygen sources is set according to the analytic solution for Ficks law in 1D; thereby the oxygen concentration at the boundary is the prescribed environmental oxygen concentration and the oxygen concentration $15.9\,\mu\mathrm{m}$ into the structure is $0.0\,\mathrm{mol/mm^3}$.

6.1. Model problem

In order to isolate different model characteristics from each other, we will study a simple model problem for displaying the different effects. The model problem is a 2D structure which is shown in Fig. 3 (left). The edge length of the structure is $0.21\ \mathrm{mm}$. It consists of two rectangular grains, each with a face centered cubic (FCC) crystal structure. We adopt 12 slip systems of the type $\{1\,1\,1\}$ and $\{1\,\bar{1}\,0\}$. For demonstration purposes, the slip system orientation is mirrored along a horizontal grain boundary. The structure is exposed to an oxygen-rich environment on one or both ends of the grain boundary, depending on the test case. The deployed parameter values of the crystal plasticity model and the coupled cohesive zone model are given in Table 1 in Appendix C. Parameter values are chosen such that a qualitatively reasonable model behavior is obtained.

The structure is exposed to displacement or force driven mechanical loading. It is found in experiments that pre-oxidation at high temperatures without mechanical loading does not influence the material behavior significantly (Liu and White, 1987). Motivated by this, we define two main loading scenarios as shown in Fig. 3 (right). In scenario (a), the mechanical load is increased linearly during a load time t_{load}, followed by a dwell time t_{dwell}. In scenario (b) the order of loading and dwelling is changed, corresponding to pre-oxidation as described by Liu and White (1987). For comparison, two additional scenarios are included, where the structure is loaded without any dwell time in vacuum, (c), or in an oxygen-rich environment, (d). For examining the ultimate tensile strength in the different scenarios, they are complemented by loading the structure to material failure.

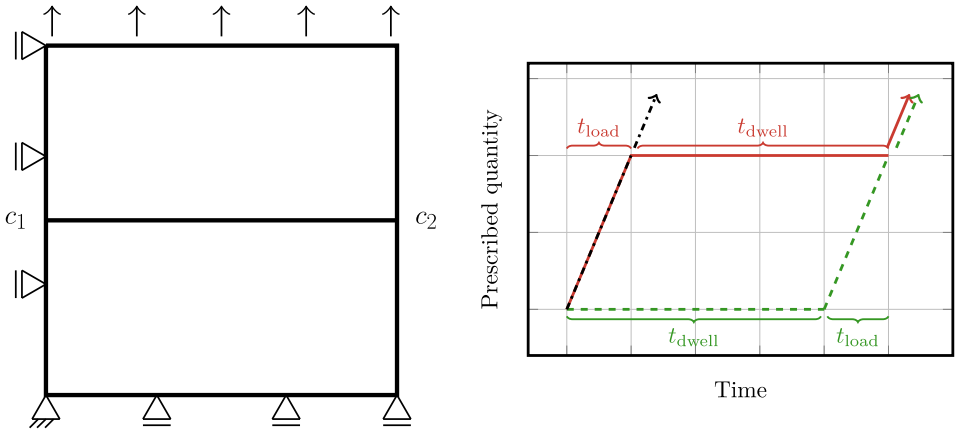

Fig. 3. Two main loading scenarios are used, which can be conducted under force or displacement control: (a) The structure is loaded mechanically and then exposed to a dwell time in an oxygen-rich environment (red/solid); (b) the structure is (without mechanical loading) exposed to an oxygen rich environment and loaded afterwards (green/dashed). Additionally, two scenarios without dwell time are considered: (c) loading in vacuum without dwell time; (d) loading in an oxygen-rich environment without dwell time (here both in black/dash-dotted). All scenarios can be extended by fully loading the structure up to failure at the end of the loading curve (indicated by arrows).

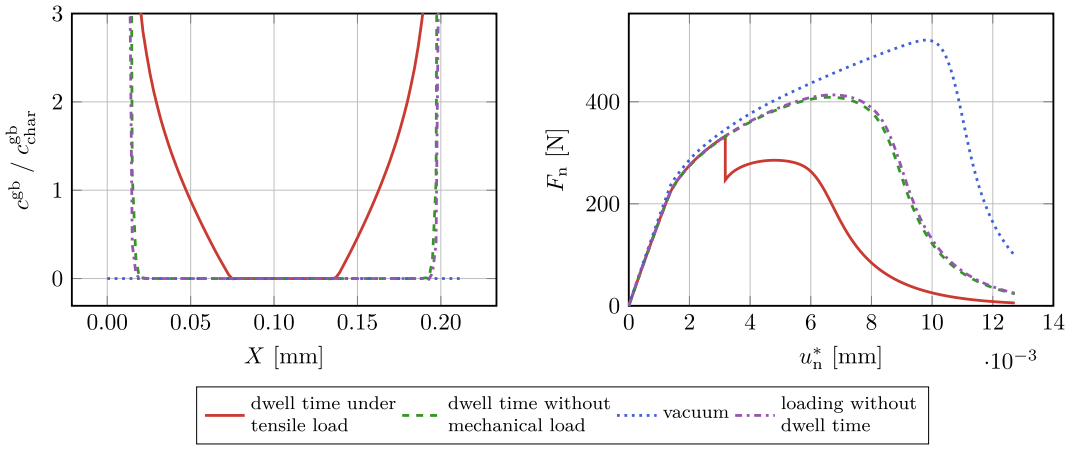

Fig. 4. Right: Reaction force F_{n} curves for the model problem by displacement controlled mode-1 fracture in the 4 different loading scenarios. Loading scenario (a) leads to a significant drop of the ultimate tensile strength compared to the other scenarios. Left: Oxygen distributions along the grain boundary (which coincides with the X-coordinate) after loading and dwelling (scenario (a) and (b)) or after loading (scenario (c) and (d)). Scenario (a) shows a considerably higher amount of oxygen in the grain boundary than the other scenarios.

6.1.1. Reduction of ultimate tensile strength

In order to observe the ultimate tensile strength of the model problem, it is loaded in displacement control. The prescribed displacement at the upper edge u^*_{n}, is increased linearly during a 15 s load time t_{load} such that the structure becomes vertically strained to 1.5%. Both sides of the grain boundary are exposed to an oxygen supply which corresponds to the amount of oxygen in environmental air at 700 °C, i.e. the concentrations c_1 and c_2 are prescribed such that $c_1 = c_2 = 2.63 \cdot 10^{-9}\,\text{mol/mm}^3$ during a dwell time of $t_{\text{dwell}} = 6\,\text{h}$.

Fig. 4 shows the normalized oxygen concentration $c^{\text{gb}} / c^{\text{gb}}_{\text{char}}$ along the grain boundary and reaction force–displacement curves for all loading scenarios. For scenario (a) and (b), the oxygen concentrations after the combination of load and hold time are shown. For scenario (c) and (d), the concentration distribution after loading is displayed. Note that the vertical axis is for clarity of presentation cut off at a normalized oxygen concentration of 3. A higher oxygen concentration does not lead to a significantly increased environmental damage.

Loading scenario (a) causes significantly higher oxygen concentrations in the structure than loading scenario (b). The oxygen diffusion during the dwell time goes along with a reduction of the normal reaction force and ultimately results in a significantly lower ultimate tensile strength for scenario (a) than for scenario (b). Notice that scenario (b) and (d) lead to similar results, thus a dwell time without mechanical loading does not have a significant impact on the model behavior. Scenario (c) leads to a significantly higher ultimate tensile strength. However, the main reason for this is that a small initial oxygen concentration is prescribed near

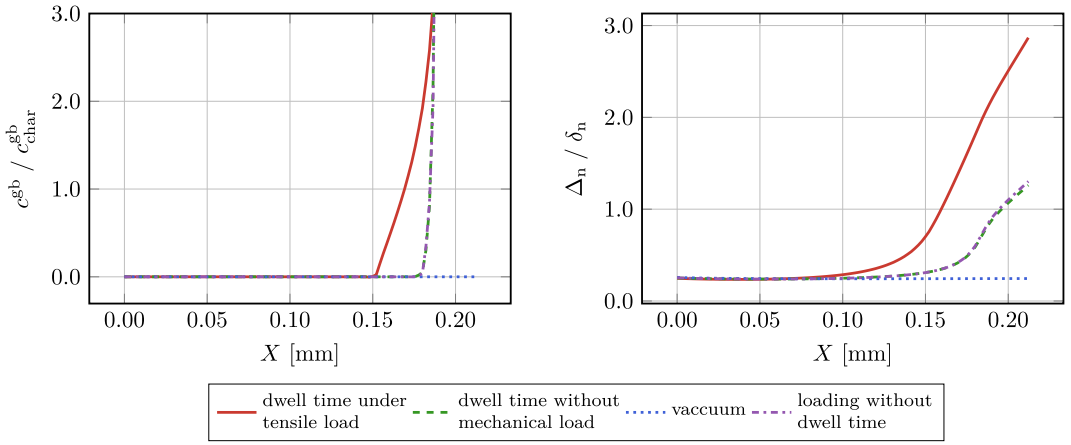

Fig. 5. Normalized oxygen and normal separation distributions after 1.5 h dwell time. Scenario (a) leads to the highest oxygen concentrations as well as to the largest normal separation jumps.

the boundaries in the first three loading scenarios for numerical reasons, which, unlike in vacuum, leads to an initial damage in the grain boundary.

The need to prescribe an initial oxygen concentration stems from the large difference between the environmental oxygen concentration and the initial zero-oxygen concentration in the grain boundaries. In theory, this leads to an infinite concentration gradient. In practice, the concentration gradient that needs to be captured depends on the chosen time step. A finer mesh size is required for a shorter time step. If the mesh is not sufficiently fine for capturing the concentration gradient, numerical oscillations occur and lead to (unphysical) negative concentrations. Similar numerical problems have been observed in the past, e.g. by Sofronis and McMeeking (1989). We circumvent this problem by prescribing an initial oxygen distribution close to the boundary. Notice that as the structure in the model problem is small, the portion of the grain boundary that is predamaged by oxygen is comparatively large and thus we see a significant difference between the ultimate tensile strength of environmentally predamaged structures and undamaged structures in Fig. 4. For larger structures, the ratio between the environmentally predamaged area and the total interface area decreases and the reduction of ultimate tensile strength is expected to be negligible. Furthermore, we expect that a steep, but smooth transition from the environmental oxygen concentration to the much lower oxygen concentration in the grain boundaries represents a physically more realistic case than an instantaneous jump of the concentration at the boundary.

6.1.2. Accelerated crack growth

A common observation in nickel-based superalloys at high temperatures is that crack growth in oxygen-rich environments (after dwelling) is accelerated compared to crack growth in vacuum. We use the normal separation jump in the interface as a measure for showing this property. The model problem is therefore loaded under force control by ramping up the load during a load time $t_{load} = 13\,s$ until a maximum prescribed traction at the upper side of the structure of 1300 MPa is reached. Under force control, the total prescribed load has to be carried by the remaining part of the grain boundary as the crack progresses during the dwell time, leading to a larger resulting load on the unbroken part. This is opposed to the displacement controlled loading scenario, in which the resulting force decreases during the dwell time. The problem at hand is therefore considerably more sensitive to force controlled loading than to displacement controlled loading. Hence, the dwell time is reduced to $t_{dwell} = 1.5\,h$. Oxygen is supplied only from the right hand side by the amount of oxygen in environmental air, i.e. $c_2 = 2.63 \cdot 10^{-9}\,mol/mm^3$. Fig. 5 shows the normalized oxygen distribution and the normalized separation jump along the interface at the end of the dwell time for scenario (a) and (b) and after loading for scenario (c) and (d), respectively.

Similarly to the results in the previous section, oxygen diffuses further into the grain boundary in scenario (a), than in case (b). Subsequently, scenario (a) leads to the largest separation jump at the right side of the structure. Again, scenario (b) and (d) experience similar behavior, indicating that dwelling without loading does not notably damage the material. A dwell time under tensile loading as for scenario (a), however, causes a larger normal separation jump than in the other scenarios. Further, notice that a normalized normal separation of 1.0 corresponds to the beginning of the softening region of the material, i.e. while the right side of the grain boundary just starts to break in scenario (b), it has already experienced significant deterioration in scenario (a). We therefore conclude that scenario (a) causes faster crack growth than scenarios (b) and (d).

6.1.3. Saturation behavior

For very high and very low environmental oxygen pressures, saturation of the crack growth speed has been experimentally observed, see e.g. Molins et al. (1997), Moverare and Gustafsson (2011). Likewise, faster material relaxation has in Pfaendtner and McMahon (2001) been observed for higher environmental pressures. Here, we reproduce this effect on the model problem under displacement control and show that the relaxation effect underlies saturation behavior for high environmental oxygen

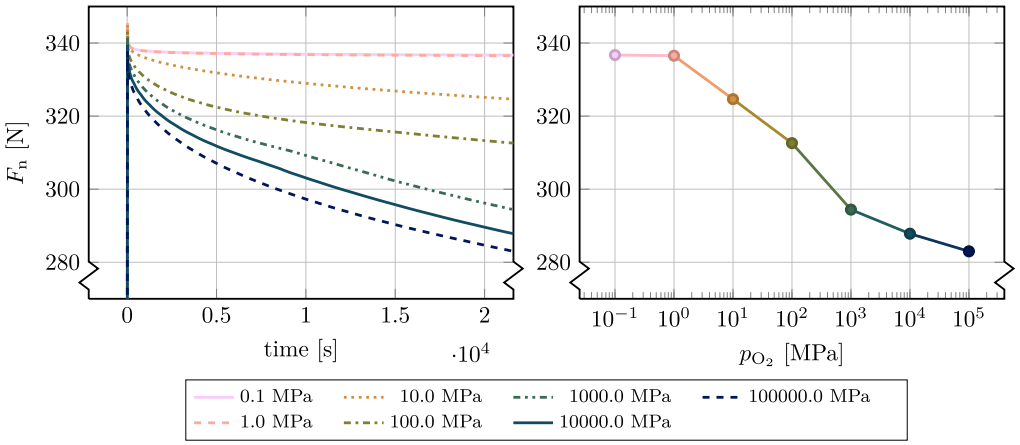

Fig. 6. Left: Reaction force F_n relaxation under displacement control for varying environmental oxygen concentration. 21278 Pa corresponds to the partial oxygen pressure in environmental air at 700 °C. Right: Reaction force after the 6 h dwell time as a function of the environmental oxygen pressure p_{O_2}.

concentrations. The model problem is loaded by ramping up the displacement up to 1.5% vertical strain of the structure followed by dwelling for 6 h. Oxygen is supplied to the structure only from the right side of the grain boundary. The environmental oxygen level varies between a partial oxygen pressure of 0.1 MPa, i.e. $c_2 = 1.236 \cdot 10^{-14}$ mol/mm^3 and 100 000 MPa, i.e. $c_2 = 1.236 \cdot 10^{-8}$ mol/mm^3. The oxygen concentrations are computed from the pressure levels by the ideal gas law at 700 °C. Fig. 6 displays relaxation curves for different levels of environmental oxygen pressure. For increasing external oxygen pressure, the reaction force is decreasing. Note that differences between the oxygen levels decrease for increasing pressure. On the right hand side of Fig. 6, the reaction forces after 6 h of dwell time are plotted versus their corresponding environmental oxygen pressure levels. For low environmental oxygen concentration there is no change in the reaction force. This is the case when the boundary concentration is significantly lower than the characteristic oxygen concentration c^{gb}_{char} for environmental damage. This corresponds well to experimental results, where for these cases crack growth is likely to happen trans- and not intergranular. For high environmental oxygen concentrations, we can observe a saturation effect in the reaction force drop. Namely, the decrease in reaction force on a logarithmic scale is steeper below approximately 10^3 MPa, than above 10^3 MPa.

6.2. Polycrystalline example

Polycrystals experience significantly more complex loading conditions and diffusion patterns than the presented model problem. To illustrate this, we will analyze loading scenario (a) and (b) on a polycrystal with a stress concentration. Fig. 7 shows the polycrystalline structure and the applied boundary conditions. The polycrystalline structure is generated by Neper (Quey et al., 2011). The structure is simply supported on the bottom and the left side, the upper edge is loaded by prescribing its normal displacement to u^*_n, whereby the structure is vertically strained up to 2% during a load time $t_{load} = 20$ s. The right edge is exposed to environmental air, while all other boundaries are considered as inside further material, i.e. $c_1 = 0$ mol/mm^3, while $c_2 = 2.63 \cdot 10^{-9}$ mol/mm^3. The dwell time is $t_{dwell} = 69.44$ h. The grains are assigned distinct random crystal lattice orientations (with FCC-slip systems). The employed crystal orientations are given in Appendix C.

In reality, polycrystals often experience material inhomogeneities that can lead to stress concentrations on the micro level. Large traction gradients accelerate the oxygen diffusion in the presented model. We want to capture an inhomogeneity in this example in order to clearly demonstrate this property. Note that a, however smaller, acceleration of oxygen diffusion would be observable even without the introduced stress concentration due to the internal state of the structure (traction gradients result from environmental damage by natural oxygen diffusion as well as from the different crystal orientations of the grains). To obtain a stress concentration, the hatched (green) grain is assigned a higher resolved yield stress of $\tau_y = 5000$ MPa, such that it will in practice behave elastically. In Fig. 8 oxygen distributions after loading and dwelling, i.e. at $t = t_{load} + t_{dwell}$ for loading scenario (a) (left side) and loading scenario (b) (right side) are displayed. It is noticeable how oxygen diffusion has advanced significantly further into the structure in scenario (a) than scenario (b). The difference between the loading scenarios is caused by traction assisted diffusion that happens in case (a), but not in case (b) due to the absence of normal traction during the dwell time. We can further observe larger separation between the grain boundaries in scenario (a) than for scenario (b). This is mainly true for the regions that experience higher oxygen levels in scenario (a) than in scenario (b). Thus, an acceleration of crack growth is to expected for dwelling under tensile load as opposed to dwelling without tensile load or to the case of no oxygen in the grain boundaries.

In Fig. 9 the mechanical behavior of the polycrystal is displayed. On the left side, the relaxation behavior during the dwell time in load case (a) is shown. We can observe an increasing drop of the reaction force at the upper edge as the oxygen diffuses into the structure. On the right hand side, the reaction force displacement curves show similar behavior for both loading cases. The 69.44 h-exposure of the structure to oxygen in loading scenario (b) does not cause any distinct change to the force displacement response when loading.

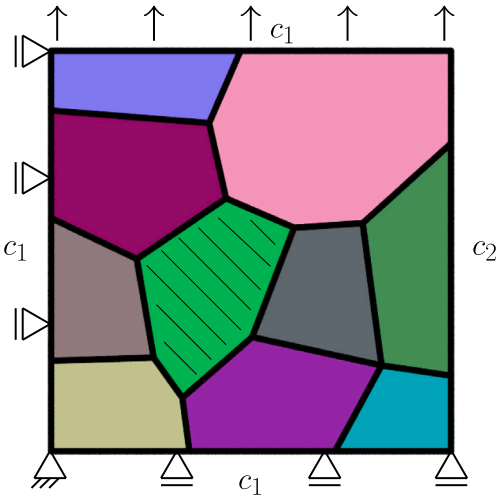

Fig. 7. Polycrystalline structure with boundary conditions. The structure is simply supported on the bottom and left edge, the upper edge is loaded in displacement control. Oxygen is supplied only on the right side with a boundary concentration c_2 ($c_1 = 0\,\mathrm{mol/mm^3}$). The hatched (green) grain is assigned a higher resolved yield stress τ_y, such that it in practice behaves linear elastically, which leads to a stress concentration in the grain structure.

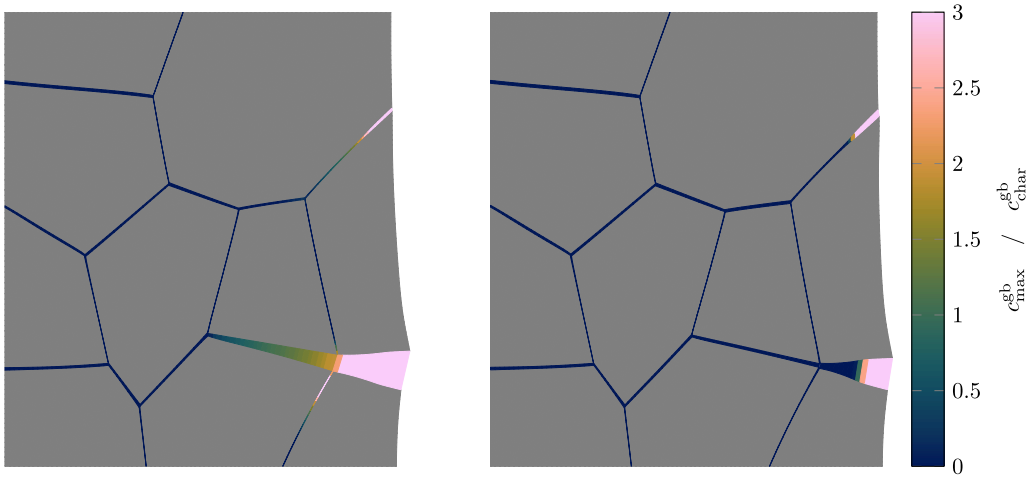

Fig. 8. Oxygen distribution after the dwell time for loading scenario (a) on the left and loading scenario (b) on the right. Displacements are magnified by factor 5. Traction assisted diffusion leads to significantly higher oxygen concentrations when dwelling happens under tension loading.

6.3. A remark on inter- versus transgranular fracture

The cracking behavior of nickel-based superalloys at high temperatures changes from ductile transgranular fracture in vacuum to brittle intergranular fracture in oxygen rich environments (see e.g. Molins et al. (1997)). In this work, a model for intergranular fracture has been presented. It does not allow for transgranular fracture and thus does not cover the transitioning range between trans- and intergranular fracture. Nevertheless, in this section comparisons between vacuum and oxygen rich environments were drawn. In this regard, the results for vacuum should be interpreted as an upper bound.

The authors propose the following modeling approach for incorporating transgranular fracture: Grain boundaries that are not environmentally attacked are in general stronger than the grains, thus failure occurs transgranularly. Upon oxygen embrittlement the grain boundaries are weakened. In the transitioning region between trans- and intergranular fracture, the ultimate strength of the grain boundaries and the grains is approximately equal; Complex stress states in polycrystals additionally support that both types of fracture may occur. After the transitioning region, the grain boundaries are clearly weaker than the grains and thus the polycrystal breaks along the grain boundaries. Fracture through grains is often ductile and could in the future be accounted for by e.g. a phase field fracture model.

This order of events suggests that the ultimate tensile strength of the bulk material is in between the ultimate tensile strengths of the damaged and undamaged grain boundaries. Therefore, the ultimate tensile strength in vacuum (without environmental damage) that is presented in the results is an upper bound for the actual ultimate tensile strength of the material.

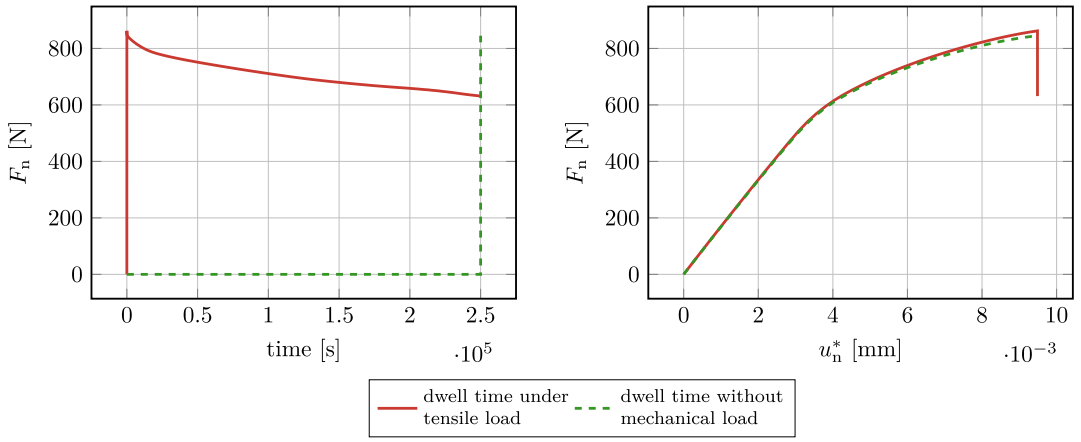

Fig. 9. Reaction force F_n at the upper edge of the polycrystalline structure. Left: Relaxation behavior; Right: Reaction-force displacement curves. The loading curves for both scenarios are similar, thus dwelling without mechanical loading does not change the behavior of the structure.

7. Concluding remarks

In this paper we have proposed a fully chemo-mechanically coupled cohesive zone model for the interaction of oxygen diffusion and crack propagation along grain boundaries. We have shown by numerical simulations that the model can predict experimental observations caused by interaction between mechanical loading and the presence of oxygen in the grain boundaries. As the presented model is based on experimental observations, it is valid independently of the underlying chemical process (such as SAGBO or dynamic embrittlement). Examples of such observations and effects which are shown in the numerical simulations are: a reduction of ultimate tensile strength, accelerated crack growth, accelerated oxygen diffusion due to mechanical loading and saturation of crack growth dependence on environmental oxygen concentrations. The numerical model predicts a distinct difference in the oxygen diffusion between dwelling with and without mechanical loading. The numerical simulations have mainly been conducted on a model problem with two grains and a single grain boundary to show the model features in a clear way. In addition to the two-grain example, the chemo-mechanically coupled problem in the grain boundaries has also been analyzed by simulations of a polycrystalline model. In these simulations, the effect of mechanical loading during dwelling on the diffusion of the oxygen as well as on the crack propagation has been shown.

A numerical framework for the implementation of the chemo-mechanically coupled cohesive zone model in finite element software has been presented. A chemo-mechanically coupled cohesive element that allows the concentration and the displacement field to share nodes and integration points is suggested. This introduces an extra but small computational cost for solving the diffusion problem in the direction normal to the grain boundaries. However, it allows the usage of a single mesh with classical cohesive elements and thus avoid defining and mapping a lower-dimensional mesh for diffusion.

The chemo-mechanically fully coupled cohesive zone model is described within a thermodynamical framework. The cohesive zone model allows for a realistic irreversible mechanical behavior for cyclic loading. In this work simulations of cyclic loading have not been included, but they are a possible investigation in future work. The consistency of the framework has been analyzed and most terms arising from the framework fulfill the 2nd law of thermodynamics individually.

Simulations in this work have been conducted for 2D grain structure models in order to study the model behavior with reasonable CPU-time. However, the proposed model formulation and the numerical framework allow for a straightforward extension to simulations of 3D grain structure models. To accomplish this, we will in future work improve the efficiency of the numerical implementation. This will enable quantitative comparisons, parameter identification and validation against experimental data. Also, investigations of grain-size dependence, including the Hall-Petch effect, would be possible in future work.

CRediT authorship contribution statement

Kim Louisa Auth: Methodology, Software, Investigation, Data curation, Writing – original draft, Writing – review & editing, Visualization. **Jim Brouzoulis:** Methodology, Writing – review & editing, Supervision. **Magnus Ekh:** Methodology, Conceptualization, Writing – original draft, Writing – review & editing, Supervision, Funding acquisition.

Declaration of competing interest

The authors declare that they have no known competing financial interests or personal relationships that could have appeared to influence the work reported in this paper.

Acknowledgments

The work in this paper has been funded by the Swedish Research Council (Vetenskapsrådet) under the grant numbers 2018-04318 and 2018-06482. The majority of the simulations were performed on resources at the Chalmers Centre for Computational Science and Engineering (C3SE) provided by the Swedish National Infrastructure for Computing (SNIC).

Appendix A. Thermodynamic consistency

It remains to check that the suggested free energy is thermodynamically consistent. As previously discussed, this means fulfilling Eq. (18). The terms for the five damage variables are

$$-\frac{\partial \Psi_{\Gamma_s}}{\partial d_n}\dot{d}_n = \mathcal{H}\left(\Delta_n\right)\left(1-d_{O_2}\,\mathcal{H}\left(\Delta_n\right)\right)\frac{\Phi_n}{\delta_n^2}\left(1-d_{c,t}\,\mathcal{H}\left(\Delta_n\right)\right)\left(\frac{\Delta_n}{2}-V_{O_2}\left(c^{gb}-c_0^{gb}\right)\right)\Delta_n\,\dot{d}_n \tag{63}$$

$$-\frac{\partial \Psi_{\Gamma_s}}{\partial d_{c,t}}\dot{d}_{c,t} = \mathcal{H}\left(\Delta_n\right)\left(1-d_{O_2}\,\mathcal{H}\left(\Delta_n\right)\right)\frac{\Phi_n}{\delta_n^2}\left(1-d_n\,\mathcal{H}\left(\Delta_n\right)\right)\left(\frac{\Delta_n}{2}-V_{O_2}\left(c^{gb}-c_0^{gb}\right)\right)\Delta_n\,\dot{d}_{c,t} \tag{64}$$

$$-\frac{\partial \Psi_{\Gamma_s}}{\partial d_t}\dot{d}_t = \left(1-d_{O_2}\,\mathcal{H}\left(\Delta_n\right)\right)\frac{1}{2}\frac{\Phi_t}{\delta_t^2}\left(1-d_{c,n}\right)\boldsymbol{\Delta}_t\cdot\boldsymbol{\Delta}_t\,\dot{d}_t \tag{65}$$

$$-\frac{\partial \Psi_{\Gamma_s}}{\partial d_{c,n}}\dot{d}_{c,n} = \left(1-d_{O_2}\,\mathcal{H}\left(\Delta_n\right)\right)\frac{1}{2}\frac{\Phi_t}{\delta_t^2}\left(1-d_t\right)\boldsymbol{\Delta}_t\cdot\boldsymbol{\Delta}_t\,\dot{d}_{c,n} \tag{66}$$

$$-\frac{\partial \Psi_{\Gamma_s}}{\partial d_{O_2}}\dot{d}_{O_2} = \mathcal{H}\left(\Delta_n\right)\left[K_n\left(\frac{\Delta_n}{2}-V_{O_2}\left(c^{gb}-c_0^{gb}\right)\right)\Delta_n+\frac{1}{2}K_t\,\boldsymbol{\Delta}_t\cdot\boldsymbol{\Delta}_t\right]\dot{d}_{O_2}\,. \tag{67}$$

The only case for which some of the above expressions can become smaller than zero is if $\Delta_n < 2\,V_{O_2}\left(c^{gb}-c_0^{gb}\right)$. This is true only for very small normal separation jumps in the presence of high oxygen concentration.

Appendix B. Coupled cohesive elements

We will term by term introduce the expressions for c and δc (Eqs. (49) and (51), respectively) into Eq. (54) for showing how it can be reformulated into two residual vectors.

After splitting the volume integral over Ω_s into an integral over the mid-plane Γ_s and an integral over the out-of-plane coordinate ξ_3, the first term of Eq. (54) becomes

$$\begin{aligned}\int_{\Omega_s}\dot{c}\,\delta c\,\mathrm{d}V &= \int_{\Gamma_s}\int_{-\frac{h}{2}}^{\frac{h}{2}}\left(\dot{c}^{mid}+\Delta\dot{c}\,\frac{\xi_3}{h}\right)\left(\delta c^{mid}+\delta\Delta c\,\frac{\xi_3}{h}\right)\mathrm{d}\xi_3\,dA\\ &= \int_{\Gamma_s}\left(h\,\dot{c}^{mid}\right)\delta c^{mid}\,\mathrm{d}A+\frac{h}{12}\int_{\Gamma_s}\Delta\dot{c}\,\delta\Delta c\,\mathrm{d}A\,.\end{aligned} \tag{68}$$

For integrating the second term over the ξ_3-coordinate, we need to find an explicit expression for $\boldsymbol{j}(\xi_3)$. The flux $\boldsymbol{j}$ (Eq. (34)) can in a 3D setting be expressed as

$$\boldsymbol{j} = -D\,\boldsymbol{\nabla}c+D\,\frac{V_{O_2}}{T\,R}\,c\,\boldsymbol{\nabla}^{gb}\hat{T}_n\,. \tag{69}$$

Notice that the gradient operator in the second term of Eq. (69) is the in-plane gradient $\boldsymbol{\nabla}^{gb}$. This is because the cohesive traction is only defined on the mid-surface of the interface domain, therefor it does not make sense to take the gradient of it perpendicular to the mid-surface. $\hat{T}_n$ is assumed to depend only on the in-plane coordinates: $\hat{T}_n = \hat{T}_n\left(\xi_1,\,\xi_2\right)$.

Analogously to the in-plane gradient operator $\boldsymbol{\nabla}^{gb}$, we define the out-of-plane gradient operator as $\boldsymbol{\nabla}_\perp = \left(\tilde{\boldsymbol{n}}^{gb}\otimes\tilde{\boldsymbol{n}}^{gb}\right)\cdot\boldsymbol{\nabla}$. Thus the gradient can be expressed as $\boldsymbol{\nabla} = \boldsymbol{\nabla}^{gb}+\boldsymbol{\nabla}_\perp$, where in the local coordinate system $\boldsymbol{\xi}$, the gradient operators are given by

$$\boldsymbol{\nabla}^{gb} = \begin{bmatrix}\frac{\partial}{\partial\xi_1}\\ \frac{\partial}{\partial\xi_2}\\ 0\end{bmatrix},\quad \boldsymbol{\nabla}_\perp = \begin{bmatrix}0\\ 0\\ \frac{\partial}{\partial\xi_3}\end{bmatrix}. \tag{70}$$

By inserting Eq. (49) into Eq. (69) and adopting the additive split of the gradient operator $\boldsymbol{\nabla}$, we obtain the dependency of the flux on the ξ_3-coordinate

$$\boldsymbol{j} = -D\left(\boldsymbol{\nabla}^{gb}\,c^{mid}+\boldsymbol{\nabla}^{gb}\,\Delta c\,\frac{\xi_3}{h}+\frac{\Delta c}{h}\,\tilde{\boldsymbol{n}}^{gb}\right)+D\,\frac{V_{O_2}}{T\,R}\left(c^{mid}+\Delta c\,\frac{\xi_3}{h}\right)\boldsymbol{\nabla}^{gb}\hat{T}_n\,. \tag{71}$$

Table 1
Material parameter values employed for the numerical experiments. The values have been chosen such that qualitatively reasonable model behavior is obtained.

Parameter		Value	Unit
Young's modulus	E	$200 \cdot 10^3$	MPa
Poisson's ratio	ν	0.3	–
Resolved yield stress	τ_y	500	MPa
Isotropic hardening modulus	H_{iso}	$10 \cdot 10^3$	MPa
Kinematic hardening modulus	H_{kin}	$30 \cdot 10^3$	MPa
Saturation stress for kinematic hardening	β_∞	150	MPa
Visco-plastic relaxation time	t^*	15	s
Visco-plastic drag stress	σ_d	50	MPa
Visco-plastic exponent	m	10	–
Normal strength	$\sigma_{\max}$	$2 \cdot 10^3$	MPa
Tangential strength	$\tau_{\max}$	$2 \cdot 10^3$	MPa
Characteristic normal separation	δ_n	$1.5 \cdot 10^{-3}$	mm
Characteristic tangential separation	δ_t	$1.5 \cdot 10^{-3}$	mm
Diffusion coefficient	D	$1 \cdot 10^{-10}$	$\text{mm}^2\,\text{s}^{-1}$
Partial molar volume of oxygen	V_{O_2}	$79.29 \cdot 10^3$	$\text{mm}^3\,\text{mol}^{-1}$
Characteristic grain boundary concentration	c^{gb}_{char}	$0.1 \cdot 10^{-15}$	$\text{mol}\,\text{mm}^{-2}$
Maximum environmental damage	$d_{O_2,\max}$	0.8	–
Cohesive zone thickness	h	$0.1 \cdot 10^{-3}$	mm

Table 2
Rodrigues vectors employed in the polycrystalline example.

Grain	Rodrigues vectors		
1	−3.666	2.537	−0.518
2	3.802	22.400	16.745
3	−6.323	5.625	−27.730
4	−0.221	0.255	−0.097
5	0.083	0.536	0.016
6	1.124	−1.052	−1.098
7	1.397	2.074	−0.645
8	0.550	−0.526	−0.546
9	0.706	−0.940	1.024
10	−0.971	−0.424	0.367

Subsequently, integrating the second term of Eq. (54) over the ξ_3-coordinate yields

$$\begin{aligned}\int_{\Omega_s} \boldsymbol{j}\cdot\boldsymbol{\nabla}\delta c\,\mathrm{d}V = &\int_{\Gamma_s}\left[-D\,\boldsymbol{\nabla}^{gb}(h\,c^{mid}) + D\,\frac{(h\,\Delta c)}{h}\,\tilde{\boldsymbol{n}}^{gb} + \frac{D\,V_{O_2}}{R\,T}\,(h\,c^{mid})\boldsymbol{\nabla}^{gb}\hat{T}_n\right]\cdot\boldsymbol{\nabla}^{gb}\delta c^{mid}\,\mathrm{d}A\\ &+\int_{\Gamma_s}\left[\frac{1}{h}\left(-D\,\boldsymbol{\nabla}^{gb}(h\,c^{mid}) + D\,\frac{(h\,\Delta c)}{h}\,\tilde{\boldsymbol{n}}^{gb} + \frac{D\,V_{O_2}}{R\,T}\,(h\,c^{mid})\boldsymbol{\nabla}^{gb}\hat{T}_n\right)\cdot\tilde{\boldsymbol{n}}^{gb}\,\delta\Delta c\right.\\ &\left.+\frac{1}{12}\left(-D\,\boldsymbol{\nabla}^{gb}(h\,\Delta c) + \frac{D\,V_{O_2}}{R\,T}\,(h\,\Delta c)\boldsymbol{\nabla}^{gb}\hat{T}_n\right)\cdot\boldsymbol{\nabla}^{gb}\delta\Delta c\right]\mathrm{d}A\,.\end{aligned} \tag{72}$$

Notice that $\tilde{\boldsymbol{n}}^{gb}$ is a unit vector and therefor $\tilde{\boldsymbol{n}}^{gb}\cdot\boldsymbol{\nabla}^{gb} = 0$. The third term of Eq. (54) is an integral over the boundary of Ω_s. We assume a zero-flux boundary condition on the boundaries between the interfaces and the grains. Further, on the boundaries $\partial\Gamma_s$ we set $\Delta c = 0$, i.e. the concentration field and thus the flux are independent of ξ_3. Therefor, integrating the third term over ξ_3 leads to

$$\int_{\partial\Omega_s} j^*\,\delta c\,\mathrm{d}A = \int_{\partial\Gamma_s} h\,j^*\,\delta c^{mid}\mathrm{d}S\,. \tag{73}$$

Finally, since the variations δc^{mid} and $\delta\Delta c$ are arbitrary, the weak form of the mass balance can be separated into two uncoupled parts: one referring to the mid-plane concentration and one referring to the concentration jump. Under consideration of Eqs. (52) and (53), we obtain the uncoupled weak forms shown in Eqs. (55) and (56).

Appendix C. Material parameters values

The deployed material parameter values for the numerical examples are shown in Table 1. The crystal orientations of the grains are randomly generated by Neper. The orientations employed for the polycrystalline example in Section 6.2 are given by Table 2. The grains are numbered as shown in Fig. 10.

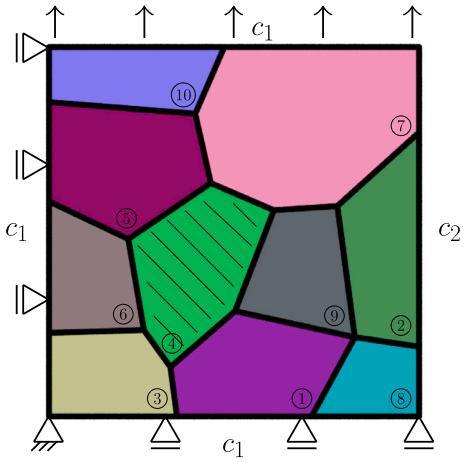

Fig. 10. Grain numbering in the polycrystalline example. The corresponding Rodrigues vectors are given in Table 2.

References

Andrieu, E., Molins, R., Ghonem, H., Pineau, A., 1992. Intergranular crack tip oxidation mechanism in a nickel-based superalloy, vol. 154. (ISSN: 09215093) pp. 21–28.

Bai, Yang, Zhao, Kejie, Liu, Yao, Stein, Peter, Xu, Bai Xiang, 2020. A chemo-mechanical grain boundary model and its application to understand the damage of Li-ion battery materials. Scr. Mater. (ISSN: 13596462) 183, 45–49. http://dx.doi.org/10.1016/j.scriptamat.2020.03.027.

Bezanson, Jeff, Edelman, Alan, Karpinski, Stefan, Shah, Viral B., 2017. Julia: A fresh approach to numerical computing. SIAM Rev. (ISSN: 00361445) 59 (1), 65–98. http://dx.doi.org/10.1137/141000671.

Bricknell, R.H., Woodford, D.A., 1981. Grain boundary embrittlement of the iron-base superalloy in903a. Metall. Trans. A, Phys. Metall. Mater. Sci. (ISSN: 03602133) 12 A (9), 1673–1680. http://dx.doi.org/10.1007/BF02643573.

Carlsson, Kristoffer, Ekre, Fredrik, 2019. Tensors.jl - tensor computations in Julia. J. Open Res. Softw. (ISSN: 20499647) 7 (1), 2–6. http://dx.doi.org/10.5334/jors.182.

Carlsson, Kristoffer, Ekre, Fredrik, Contributors, 2021. Ferrite.jl - Finite element toolbox for Julia, https://github.com/Ferrite-FEM/Ferrite.jl.

Chang, K.M., Henry, M.F., Benz, M.G., 1990. Metallurgical control of fatigue crack propagation in superalloys. JOM (ISSN: 10474838) 42 (12), 29–35. http://dx.doi.org/10.1007/BF03220467, URL https://link.springer.com/article/10.1007/BF03220467.

Christ, H.J, Wackermann, K., Krupp, U., 2016. Materials at high temperatures effect of dynamic embrittlement on high temperature fatigue crack propagation in IN718-experimental characterisation and mechanism-based modelling effect of dynamic embrittlement on high temperature fatigue crack propagation. (ISSN: 1878-6413) http://dx.doi.org/10.1080/09603409.2016.1187464, URL https://www.tandfonline.com/action/journalInformation?journalCode=ymht20.

del Busto, Susana, Betegón, Covadonga, Martínez-Pañeda, Emilio, 2017. A cohesive zone framework for environmentally assisted fatigue. Eng. Fract. Mech. (ISSN: 00137944) 185, 210–226. http://dx.doi.org/10.1016/j.engfracmech.2017.05.021.

Di Leo, Claudio V., Anand, Lallit, 2013. Hydrogen in metals: A coupled theory for species diffusion and large elastic-plastic deformations. Int. J. Plast. (ISSN: 07496419) 43, 42–69. http://dx.doi.org/10.1016/j.ijplas.2012.11.005.

Gurtin, Morton E., Fried, Eliot, Anand, Lallit, 2010. The Mechanics and Thermodynamics of Continua. Cambridge University Press, http://dx.doi.org/10.1017/cbo9780511762956.

Hörnqvist, Magnus, Viskari, Leif, Moore, Katie L., Stiller, Krystyna, 2014. High-temperature crack growth in a Ni-base superalloy during sustained load. Mater. Sci. Eng. A (ISSN: 09215093) 609, 131–140. http://dx.doi.org/10.1016/j.msea.2014.04.102.

Karabela, A., Zhao, L.G., Lin, B., Tong, J., Hardy, M.C., 2013. Oxygen diffusion and crack growth for a nickel-based superalloy under fatigue-oxidation conditions. Mater. Sci. Eng. A (ISSN: 09215093) 567, 46–57. http://dx.doi.org/10.1016/j.msea.2012.12.088.

Kolluri, M., Hoefnagels, J.P.M., Van Dommelen, J.A.W., Geers, M.G.D., 2014. Irreversible mixed mode interface delamination using a combined damage-plasticity cohesive zone enabling unloading. Int. J. Fract. (ISSN: 03769429) 185 (1–2), 77–95. http://dx.doi.org/10.1007/s10704-013-9899-z.

Kristensen, Philip K., Niordson, Christian F., Martínez-Pañeda, Emilio, 2020. A phase field model for elastic-gradient-plastic solids undergoing hydrogen embrittlement. J. Mech. Phys. Solids (ISSN: 00225096) 143, http://dx.doi.org/10.1016/j.jmps.2020.104093.

Krupp, U., 2005. Dynamic embrittlement - time-dependent quasi-brittle intergranular fracture at high temperatures. Int. Mater. Rev. (ISSN: 09506608) 50 (2), 83–97. http://dx.doi.org/10.1179/174328005X14320.

Liu, C.T., White, C.L., 1987. Dynamic embrittlement of boron-doped Ni3Al alloys at 600°c. Acta Metall. (ISSN: 00016160) 35 (3), 643–649. http://dx.doi.org/10.1016/0001-6160(87)90187-8.

Méric, L., Poubanne, P., Cailletaud, G., 1991. Single crystal modeling for structural calculations: Part 1-model presentation. J. Eng. Mater. Technol. Trans. ASME (ISSN: 15288889) 113 (1), 162–170. http://dx.doi.org/10.1115/1.2903374.

Meyer, Knut Andreas, 2020. Evaluation of material models describing the evolution of plastic anisotropy in pearlitic steel. Int. J. Solids Struct. (ISSN: 00207683) 200–201, 266–285. http://dx.doi.org/10.1016/j.ijsolstr.2020.04.037.

Molins, R., Hochstetter, G., Chassaigne, J.C., Andrieu, E., 1997. Oxidation effects on the fatigue crack growth behaviour of alloy 718 at high temperature. Acta Mater. (ISSN: 13596454) 45 (2), 663–674. http://dx.doi.org/10.1016/S1359-6454(96)00192-9.

Moverare, Johan J., Gustafsson, David, 2011. Hold-time effect on the thermo-mechanical fatigue crack growth behaviour of Inconel 718. Mater. Sci. Eng. A (ISSN: 09215093) 528 (29–30), 8660–8670. http://dx.doi.org/10.1016/j.msea.2011.08.027.

Musienko, Andrey, Cailletaud, Georges, 2009. Simulation of inter- and transgranular crack propagation in polycrystalline aggregates due to stress corrosion cracking. Acta Mater. (ISSN: 13596454) 57 (13), 3840–3855. http://dx.doi.org/10.1016/j.actamat.2009.04.035.

Ottosen, Niels Saabye, Ristinmaa, Matti, Mosler, Jörn, 2015. Fundamental physical principles and cohesive zone models at finite displacements - limitations and possibilities. Int. J. Solids Struct. (ISSN: 00207683) 53, 70–79. http://dx.doi.org/10.1016/j.ijsolstr.2014.10.020.

Pfaendtner, J.A., McMahon, Jr., J., 2001. Oxygen-induced intergranular cracking of a Ni-base alloy at elevated temperatures - an example of dynamic embrittlement. Acta Mater. (ISSN: 13596454) 49 (16), 3369–3377. http://dx.doi.org/10.1016/S1359-6454(01)00005-2.

Quey, R., Dawson, P.R., Barbe, F., 2011. Large-scale 3D random polycrystals for the finite element method: Generation, meshing and remeshing. Comput. Methods Appl. Mech. Engrg. (ISSN: 00457825) 200 (17–20), 1729–1745. http://dx.doi.org/10.1016/j.cma.2011.01.002.

Rezaei, Shahed, Asheri, Armin, Xu, Bai-Xiang, 2021. A consistent framework for chemo-mechanical cohesive fracture and its application in solid-state batteries. J. Mech. Phys. Solids (ISSN: 00225096) 157 (August), 104612. http://dx.doi.org/10.1016/j.jmps.2021.104612.

Sedlak, M., Alfredsson, B., Efsing, P., 2019. A coupled diffusion and cohesive zone model for intergranular stress corrosion cracking in 316l stainless steel exposed to cold work in primary water conditions. Eng. Fract. Mech. (ISSN: 00137944) 217 (October 2018), 106543. http://dx.doi.org/10.1016/j.engfracmech.2019.106543.

Serebrinsky, S., Carter, E.A., Ortiz, M., 2004. A quantum-mechanically informed continuum model of hydrogen embrittlement. J. Mech. Phys. Solids (ISSN: 00225096) 52 (10), 2403–2430. http://dx.doi.org/10.1016/j.jmps.2004.02.010.

Sofronis, P., McMeeking, R.M., 1989. Numerical analysis of hydrogen transport near a blunting crack tip. J. Mech. Phys. Solids (ISSN: 00225096) 37 (3), 317–350. http://dx.doi.org/10.1016/0022-5096(89)90002-1.

Sun, Yaofeng, Maciejewski, Kimberly, 2012. A damage-based cohesive zone model of intergranular crack growth in a nickel-based superalloy. 22 (6), 905–923. http://dx.doi.org/10.1177/1056789512468917.

Viskari, L., Hörnqvist, M., Moore, K.L., Cao, Y., Stiller, K., 2013. Intergranular crack tip oxidation in a Ni-base superalloy. Acta Mater. (ISSN: 13596454) 61 (10), 3630–3639. http://dx.doi.org/10.1016/j.actamat.2013.02.050.

Xu, X.P., Needleman, A., 1993. Void nucleation by inclusion debonding in a crystal matrix. Modelling Simulation Mater. Sci. Eng. (ISSN: 1361651X) 1 (2), 111–132. http://dx.doi.org/10.1088/0965-0393/1/2/001.

Zhao, L.G., 2011. Modeling of oxygen diffusion along grain boundaries in a nickel-based superalloy. J. Eng. Mater. Technol. Trans. ASME (ISSN: 00944289) 133 (3), 24–26. http://dx.doi.org/10.1115/1.4003777.